materials proceedings

MDPI

Proceeding Paper

The Annealing Effect of Structured Nickel Octahedra Nanoparticles on the Performance of NiO Supported in Silica in Combined Steam and Dry Reforming of a Model Biogas Mixture †

Karam Jabbour [1,*] and Anne Davidson [2]

[1] College of Engineering and Technology, American University of the Middle East, Kuwait
[2] Sorbonne Université, UPMC Université Paris 06, Laboratoire de Réactivité de Surface, 4 place Jussieu, 75005 Paris, France; email1@email.com (A.D.)
* Correspondence: karam.jabbour@aum.edu.kw
† Presented at the 4th International Online Conference on Nanomaterials, 5–19 May 2023; Available online: https://iocn2023.sciforum.net.

Highlights:

- Ni octahedra supported on silica are stable catalysts in steam biogas reforming
- During reduction, an annealing effect of NiO octahedra into Ni^0 nanorods occurs
- Shape transformation is accompanied by H_2-storage within Ni^0 layers
- Stored H_2 inhibits carbon formation/accumulation during catalysis

Abstract: The octahedral family of NiO nanoparticles is gaining significant attention as an assembly with unique physicochemical properties and outcomes in electromagnetics, shielding, and absorption. In this study, a mesoporous structured $Ni_{60\%}SiO_2$(Comm), chosen owing to its NiO species existing in an octahedral shape, was evaluated for synthesis gas (syngas: $H_{2(g)}$ and $CO_{(g)}$ mixtures) production via combined steam and dry reforming of a model biogas mixture (T = 800 °C, ($H_2O_{(g)}$ + $CO_{2(g)}$)/$CH_{4(g)}$ = 1.2). To the best of our knowledge, the consideration of Ni octahedra-based nanomaterials as potential catalysts for reforming reactions, particularly biogas reforming, towards syngas generation has not been yet considered in the available literature. In comparison to a standard $Ni_{5\%}SiO_2$ catalyst, slightly higher reactivity levels along with significantly lower amounts of carbonaceous deposits were obtained over the commercial $Ni_{60\%}SiO_2$(Comm) catalyst for 10 h on stream. The high coke resistance of originally shaped NiO octahedra was ascribed to an annealing effect, generated during $H_{2(g)}$-treatment (prior to catalysis), yielding mesoporous metallic Ni^0 nanorods with $H_{2(g)}$-storage capacities. Stored hydrogen within Ni^0 layers acted as active centers for continuous in situ coke gasification, preventing thus $C_{(s)}$ accumulation while keeping Ni^0 sites accessible for catalysis.

Keywords: octahedral nanoparticles; biogas reforming; annealing effect; carbon gasification

Citation: Jabbour, K.; Davidson, A. The Annealing Effect of Structured Nickel Octahedra Nanoparticles on the Performance of NiO Supported in Silica in Combined Steam and Dry Reforming of a Model Biogas Mixture. *Mater. Proc.* **2023**, *14*, x. https://doi.org/10.3390/xxxxx

Academic Editor(s):

Published: 5 May 2013

1. Introduction

The incessant investigation in the development of nanomaterials for various academic and industrial applications is a fundamental aspect for the improvement of science and technology [1,2]. Gaining mastery over their original shapes and over the potential textural/structural changes that might occur during application induces control over their properties and thus an enhancement in their practicality [3,4]. Particularly, the octahedral-like configuration is a platonic P4 solid characterized by 6 polyhedron apexes, 12 polyhedron edges with (110) facades and, a total of 8 identical equilateral triangle-based facets

(i.e., the (111), (101), (011) planes). The anisotropic shape along with the microstructure character of the octahedral assembly of nanomaterials were shown to deliver remarkable physicochemical properties and consequently novel catalytic outcomes owing to their surface reactivity that was shown to depend (i) on the state of the metal (i.e., oxidation number), (ii) on the degree of shape preservation during catalysis and, (iii) on the exposed facet of the nanocrystal [5–7]. For instance, when non-supported nano-octahedra $MnCr_2O_4$ based-solids with metallic tip terminations were applied for catalyzing the pitting corrosion of austenitic stainless steel in MnS inclusions; a higher overall reactivity was recorded as compared to the same crystal yet with O_2-rich terminations [8]. On the other hand, NiO octahedra converted into Ni^0 through time-dependent H_2-annealing heat treatments, at temperature values of 300, 450 and 700 °C, revealed excellent microwave absorbing performances owing to an ease in the penetration of electronic microwaves in metallic composites originating from parent octahedral-based nanostructures [3]. Then again, a change from the (100) to the (111) crystal surface of Pt_3Ni was shown beneficial in redox reactions where; a nine-fold enhancement in active surface area was recognizable to increase up to four times the activity of the octahedral nanoparticle catalyst [9]. Amongst the family of nano-octahedra materials, Ni-based ones have been extensively investigated because of their promising technological effects in a variety of applications ranging from magnetic recording media [10], magnetic sensors [11], passing to medical diagnostic equipment [12], microwave absorbing and microwave shielding materials [3,13] as well as in catalysis [9,14,15]. To the best of our knowledge, the consideration of Ni octahedra-based nanomaterials as potential catalysts for reforming reactions, particularly steam biogas reforming (SBR), towards synthesis gas (syngas: H_2 and CO mixtures) generation has not been yet considered in the available literature.

Actually, SBR is being recognized as a sustainable tactic for efficient valorization of biogases emitted from anaerobic digestion of biomass-derived organic wastes due to their composition making them attractive feedstocks for syngas production. In fact, biogas is projected to complement depleting carbon resources (coal, oil and natural gas) conventionally reconnoitered for energy generation and management [16]. Depending on the origin, biogas can have variable chemical compositions all constituted of methane (CH_4, 50–70 vol.%), carbon dioxide (CO_2, 30–40 vol.%) along with water vapor (H_2O, 20–30 vol.%) [17,18]. Conversion of these components via SBR is also referred to as combined steam and dry reforming of methane (CSDRM, $CH_4 + xH_2O + (1\text{-}x)CO_2 \leftrightarrow (2\text{-}x)CO + (2+x)H_2$), a process allowing the simultaneous consumption of CH_4 and CO_2 greenhouse gases in presence of water vapor for generation of H_2:CO mixtures with an array of molar compositions [19]. Regarding selectivity outcomes, SBR produces, in a single step, an industrially-interesting H_2:CO composition termed "metgas" (H_2:CO close to 2.0 for a CO_2+H_2O/CH_4 molar value of 1.0) [20,21]. This mixture is currently a basis for applied research since it can be valorized, without any supplementary separation units, in the generation of methanol (hence the name "metgas"), an important chemical intermediate in chemical/petrochemical industries [22]. To this end, SBR facilities are spread all around the world with an aim for high quality bio-syngas for subsequent usage in methanol synthesis, in the preparation of long hydrocarbon chains via the Fisher-Tropsch (FT) process ($(2n+1)H_2 + nCO \rightarrow C_nH_{(2n+2)} + nH_2O$) and, for upgrading into extensive range of synthetic chemicals [23]. The leading countries in Europe are Germany, UK, Italy, Czech Republic and France, with Germany accounting for almost 50% of the European Union (EU) supply [24].

In the search of catalysts for biogas transformation into syngas, supported transition metals such as Ni, Fe and/or Co dispersed over SiO_2, Al_2O_3 (and other standard oxides) stand as ideal systems achieving high conversion levels, good H_2 and CO yields and stable performances with time-on-stream (TOS) [25–28]. Specifically, intrinsic activity levels of Ni-supported catalysts, are comparable to those observed over noble metal (Ru, Rh) based-ones [29,30], reported as more resistant towards deactivation [31–33]. However,

substitution of noble by transition metals is mandatory from both economic and environmental perspectives [34,35]. Nevertheless, during endothermic biogas reforming reaction, Ni^0 nanoparticles deactivate via either coke deposition, sintering (or thermal agglomeration) or by in situ re-oxidation of reduced Ni^0 (active catalytic sites) to catalytically inactive NiO particles [36–38]. Solid carbonaceous species depositing on the inner and/or outer catalytic surface originate from side-reactions involving (i) methane hence methane decomposition (MD, $CH_4 \leftrightarrow C_{(s)} + 2H_2$), and/or (ii) CO product in a reaction termed as Boudouard reaction (BR, $2CO \leftrightarrow C_{(s)} + CO_2$). Additional (yet non-coke producing) side-reactions typically water gas-shift (WGS, $H_2O + CO \rightarrow H_2 + CO_2$) and reverse-water gas-shift (RWGS, $H_2 + CO_2 \leftrightarrow H_2O + CO$) could amend the overall selectivity of the process via the consumption/production of CO and H_2 products.

Tuning catalytic properties for increasing resistance of supported Ni^0 nanomaterials against deactivation can be manifested in various approaches one of which is the alteration of support type for enhancement of metal support interaction (MSI). The formation of a solid-solution between Ni and MgO support was found beneficial for the stabilization of the metal during SRB runs [20,21]. Likewise, hydrotalcite like-materials decomposing into mixed $MgO\text{-}Al_2O_3$ oxides as well as mixed oxides (composite-like materials) of CeO_2 and ZrO_2 stand as classical supports for Ni with high activity and selectivity in SBR [39,40]. The list of reforming catalysts based on Ni dispersed on different supports includes as well the conventional oxide that is silica, which provides considerably high initial activity levels [41] than those recorded on CeO_2 [42,43], ZrO_2 [42,43] or MgO [42] at 800 °C and for an inlet ($CO_2 + H_2O/CH_4$) molar ratio of 1.0. In addition to some patented studies, it must be pointed out that the incorporation of promoters having specific properties is another methodology for improving MSI and subsequently limiting $C_{(s)}$ deposition. One example is the study conducted by Chen et al. [41] over La_2O_3 promoted Ni/SiO_2 catalysts in SBR. The addition of 3 wt% La_2O_3 was shown to improve catalytic performance as well as coking and sintering resistances of Ni^0 nanoparticles embedded within SiO_2 matrix. The presence of the basic modifier improved dispersion, strengthened MSI and promoted the activation of CO_2 to gasify $C_{(s)}$ deposits (overall reaction: $CO_2 + C_{(s)} \rightarrow 2CO$) [44,45]. In addition to incorporation of promoters with specific properties, some of the newest strategies involve the application of structured supports such macroporous natural diatoms [46] or mesoporous SBA-15 [47–50] silicas. Despite their special textural properties in terms of (i) large specific surface area for better dispersion of Ni^0 species and (ii) well-defined porous arrangement leading to confinement effect; Ni/diatoms and Ni/SBA-15 still suffer from deactivation via re-oxidation and carbon deposition and continuous work is devoted to improve their stability under harsh SBR conditions [47–50].

An innovative approach in the direction of designing stable SRB catalysts could reside in the utilization of mesoporous octahedra-based NiO nanoparticles owing to recent (additional) characteristics found over similar phase changing materials (PCMs), typically 3D porous (3,6)-connected metal-organic frameworks [51]. It was reported that materials that undergo phase changes (known as annealing or melting effects), under different endothermic atmospheres have energy-storage potentials making them excellent candidates for drug delivery [52], smart building [53] and, solar energy systems [54]. In such systems, energy could be stored in either its thermal (heat accumulation) or chemical (hydrogen storage) form. Energy storage over methane reforming catalysts could be advantageous in terms of anti-coking especially over those having hydrogen storing capabilities. The accumulation of H_2 molecules over PCMs could facilitate the in situ gasification kinetics of $C_{(s)}$ resulting in an accessibility preservation of gaseous reactants towards Ni^0 sites.

Based on this state of the art, the aim of the present work is to check for the (potentially) positive effect of structured Ni octadehra as active sites for producing syngas under harsh biogas reforming conditions. Our goal when choosing this approach is to highlight on the effect of phase and structure changes of Ni octahedra (especially those induced by temperature augmentation under hydrogen-rich medium) and the consequences of such

modifications on physicochemical properties and subsequently on catalysis. A commercial 60 wt% Ni supported on silica (never characterized previously in literature) is chosen as a model to conduct the pilot study because of its NiO species assembling in the desired octahedral configuration. For the sake of comparison, a 5 wt% Ni impregnated on silica (Aerosil 300), obtained by the "two solvents" loading method [55,56], is adopted as standard catalyst alike those already considered in former studies. It is worth mentioning that the 5 wt% Ni/SiO_2 was applied in a preliminary study with similarly prepared silica-based catalysts notably: 5 wt% Ni/SBA-15 and 5 wt% Ni/diatoms [57]. Results showed that the Aerosil-based sample presented the highest performance with TOS while others deactivated drastically under steam biogas reforming conditions (T = 800 °C, (H_2O + CO_2)/CH_4 = 1.2, P = 1 atm).

2. Experimental

2.1. Materials and Catalyst Preparation

The 60 wt% Ni supported on silica was purchased from Sigma Aldrich (product name: nickel oxide supported on silica, # 675172) and was used as received without any purification or thermal treatment. In this study, this sample is referred to as $Ni_{60\%}SiO_2$(Comm).

Impregnation of nickel was carried out on the SiO_2 (Aerosil 300, Degussa) support using the "two solvents" technique detailed elsewhere [55,56]. Briefly, 1g of support was suspended in 35 mL of cyclohexane (C_6H_{12}, Sigma Aldrich, 17919-1) under stirring for 2–3 min. Then 0.7 mL of an aqueous nickel solution prepared using $Ni(NO_3)_2.6H_2O$ as nickel precursor in a way to contain 0.05g of Ni, was added drop-wise with the use of micropipette. The suspension was left to dry at room temperature (cyclohexane and water evaporation) without stirring before undergoing (slow) calcination in air (thin bed) at 450 °C for 5 h (heating rate 0.5 °C min^{-1}) for oxidative removal of adsorbed nitrates. The resulting sample is designated as $Ni_{5\%}SiO_2$.

2.2. Catalysts Characterizations

Nitrogen adsorption-desorption isotherms were performed on a Micromeritics ASAP 2020 instrument. Prior to measurements, samples (calcined or spent, 40 mg) were degassed under vacuum for 3 h at 300 °C then cooled down to room temperature before being placed at −196 °C (liquid nitrogen temperature). The Brunauer-Emmett-Teller (BET) surface areas were evaluated from the BET equation for a relative pressure (P/P_0) range between 0.05 and 0.25. The single point pore volume was determined from the adsorption of gaseous N_2 at exactly P/P_0 of 0.990. Pore size distribution (PSD) was calculated using the Barrett-Joyner-Halenda (BJH) method for the adsorption branch of the isotherm.

Structural characteristics of calcined, in situ reduced and spent catalysts were studied at room temperature by performing powder X-ray diffraction (XRD) at wide angles. Diffractograms were recorded on a BRUKER type D8 ADVANCE diffractometer operating at 40 kV and 30 mA and using a Cu Kα irradiation source (λ = 1.5418 Å). The acquisitions were logged for 2θ values between 10.0 to 90.0° and a step size of 0.04° (with 2s duration at each step). A comparison with standard powder XRD files published by the International Center for Diffraction Data (ICDD) helped in the identification of present crystalline phases. Crystalline domain sizes were calculated using the Scherrer equation: D (hkl) = ($K\lambda/\beta\cos\theta$), where K = 0.9 is the shape factor for spherical particles, λ is the X-ray wavelength (λ = 1.5405 nm for Cu Kα), β is the full width at half maximum (FWHM) of the diffraction peak and θ is the peak position.

The reducibility of nickel species in calcined (or commercially obtained) silica-based materials was studied by temperature programmed reduction (H_2-TPR) upon carrying the experiments on an Autochem 2920 (Micromeritics) apparatus. The unit was equipped with a thermal conductivity detector (TCD) for a continuous recording of the overall H_2 consumption. Each sample (100 mg) was deposited on a quartz wool in a U-shaped quartz reactor

and heated from room temperature to 800 °C (heating rate: 7 °C min^{-1}) under a gaseous mixture of 5 vol% H_2/Ar (30 mL min^{-1}). A bath made of ice and salt (NaCl) was used as a cold trap to condense water generated during reduction prior to the arrival of the gas for its analysis by the TCD detector. This assures that the obtained signal (difference in thermal conductivity between reference and analysis gases) is essentially linked with H_2 consumption.

The number of surface Ni sites per unit mass of catalyst (dispersion, D%) was determined by means of temperature programmed desorption (H_2-TPD) using the same unit and reactor type as those of H_2-TPR experiments. For each desorption measurement, 300 mg of sample (calcined or purchased) was first in situ reduced at 700 °C for 2 h (heating rate of 7 °C min^{-1}) under similar medium as that of H_2-TPR (5 vol% H_2/Ar, 30 mL min^{-1}). After reduction, sample was allowed to cool to 60 °C, under H_2-flow, to warrant complete saturation with hydrogen. Then, adsorbed H_2 was flushed by Ar (flow: 30 mL min^{-1}) for almost 2 h before re-heating it (still under Ar) 900 °C (heating rate: 10 °C min^{-1}). The amount of desorbed H_2 was constantly recorded, as a function of temperature, by TCD detector. The dispersion of Ni nanoparticles was calculated, based on literature [58,59], using Equation (1) where: V_{ad} (mL) represents the volume of desorbed H_2 at standard temperature and pressure (STP) conditions, M is the molecular weight of Ni (58.69 g mol^{-1}), SF is the stoichiometric factor (taken as 1), m is the weight of the sample used for analysis (0.3 g), P is the total weight fraction of Ni (5 or 60%) and V_m is the molar volume of H_2 (22.414 mL mol^{-1}) at STP. Exhaust gases were monitored and analyzed by an online gas spectrometry (MKS, Cirrus 2 mass spectrometer) by following the mass (m/z) for H_2 (2).

$$D(\%) = \frac{2 \cdot V_{ad} \cdot M \cdot SF}{m \cdot V_m \cdot P} \quad (1)$$

The morphological aspects of calcined and spent catalysts were examined by means of scanning electron microscopy (SEM). Micrographs were registered on a Hitachi SU-70 (SEM- ZEG) microscope accompanied by an energy dispersive spectroscopy (EDS) and operating with an electron acceleration tension of 7 kV.

Thermal gravimetric analysis (TGA) coupled to differential scanning calorimetry (DSC) was performed to quantify carbon deposition amounts on spent catalysts. Experiments were recorded on a TA SDT Q600 thermal analyzer instrument from RT to 900 °C (heating rate: 10 °C min^{-1}) in flowing air (50 mL min^{-1}). Exhaust gases were continuously monitored and analyzed by an online gas spectrometry (MKS, ThermoSTAR) upon following the masses (m/z) for CO (28) and CO_2 (44).

Complementary to TGA/DSC experiments, the qualification of solid $C_{(s)}$ deposits was determined via Raman spectroscopy. Spectra were collected on a KAISER (RXN1) optical system consisting of a laser with a wavelength λ of 785 nm, a microscope with an X50 long working distance (W.D. = 8.0 mm) lens and, a charge-coupled detector (CCD). The spectrometer functioned at a resolution of 4 cm^{-1} (to avoid potential fluorescence), a laser intensity of 10 mW and, for a total of 30 accumulations per spectrum (10s acquisition time).

2.3. Reactivity Measurements

The steam biogas reforming reaction was carried out at atmospheric pressure in a Microactivity (PID Eng and Tech) vertical fixed-bed continuous flow quartz reactor (internal diameter: 9 mm). Sample (200 mg non-diluted powder) was firstly in situ reduced at 650 °C for 2 h under a flow (30 mL min^{-1}) of 5 vol % H_2/Ar, in order to ensure complete reduction of NiO to Ni^0, then the flow was switched to the reactant mixture (CH_4:CO_2:H_2O:Ar = 1:0.4:0.8:12). The inlet (H_2O + CO_2)/CH_4 molar ratio was fixed at 1.2 based on performed thermodynamic and experimental studies (upon accounting for solid carbon deposition, a practical aspect that should not be ignored during reforming reactions) displaying the potential generation of "metgas" under such inlet feed composition [19,45,46,57]. Water was introduced by a HPLC pump (Gilson, USA) in the form of deionized liquid water (0.01 mL min^{-1}) that undergoes evaporation (12.3 mL min^{-1}) at 150 °C (hotbox temperature) then mixes with CH_4 and CO_2 fluxes before entering the reactor. The

total gas hourly space velocity (GHSV) was 67.7 L g_{cat}^{-1} hr^{-1}. The reaction temperature was controlled by a thermocouple placed in the middle of the catalyst bed. Catalytic measurements were carried out at 800 °C for 10 h on stream. The HSC 7.1 simulation software (H, S and C stand for enthalpy, entropy and heat capacity, respectively) was used to estimate (i) thermodynamic conversion (CH_4 and CO_2) levels and (ii) expected products (H_2 and CO) contents under applied conditions of temperature, pressure and composition (considering also dilution and carbon deposition).

Before analysis, effluent gases were passed through a gas/liquid separator to condense unreacted steam (and in situ generated amounts) in the exhaust after reaction. The dry gas (containing reactants and products) was quantified by on-line gas chromatography using a Micro-GC Inficon equipped with a thermal conductivity detector and coupled to two columns placed in parallel for the detection of CH_4, H_2 and CO (Molecular Sieve column) and of CO_2 (plot U column). For the sake of accuracy, experiments were repeated twice over each sample. The conversion fraction of CH_4 (XCH_4) and CO_2 (XCO_2) and the obtained syngas ratio (H_2:CO) were calculated according to Equations (2)–(4):

$$XCH_4 = \frac{[CH_4]_{in} - [CH_4]_{out}}{[CH_4]_{in}} \quad (2)$$

$$XCO_2 = \frac{[CO_2]_{in} - [CO_2]_{out}}{[CO_2]_{in}} \quad (3)$$

$$\frac{H_2}{CO} = \frac{\text{mol of } H_2 \text{ produced}}{\text{mol of CO produced}} \quad (4)$$

3. Results and Discussion

3.1. Morphological Characteristics of Fresh Samples

Selected SEM micrographs of calcined $Ni_{5\%}SiO_2$ (Figure 1A,B) exhibit typical silica Aerosil surface corrugations. Grains appeared as loose aggregates of small particles with a spongy appearance and irregular shapes with rough exteriors (Figure 1A). It is clear that the surface of Ni impregnated on pyrogenic silica is not completely flat and uniform rather a curvature of the surface is shown (Figure 1B), that could be related to the presence of different families of pores. Basically, those located in valleys-like forms (or cavities) (Figure 1B) are either micro-or mesopores whereas the larger category of pores (macropores) accounts essentially for the inter-granular void spaces between silica grains (as will be confirmed based on N_2-sorption isotherms). Scanning microscopy coupled to locally pointed EDS analyses reveal useful information on the dispersion of NiO nanoparticles. From such measurements performed on multiple locations, global atomic Ni/Si ratios show good homogeneity in Ni-dispersion where; the high occurrence of rich Ni-domains (Ni/Si ratios around 0.053 and 0.06) indicate that silica grains are filled with Ni. This could be due to the advantageous effects of the adopted "two solvents" method, known to facilitate metallic dispersion inside the pores during impregnation [55,56]. However, some (although few) of the calculated Ni/Si atomic ratios were in the range of 0.01, indicating that some of the grains are almost empty of Ni. Yet, considering all evaluated zones, the probability of having Ni rich domains is quite high and the degree of heterogeneity in metal distribution is low.

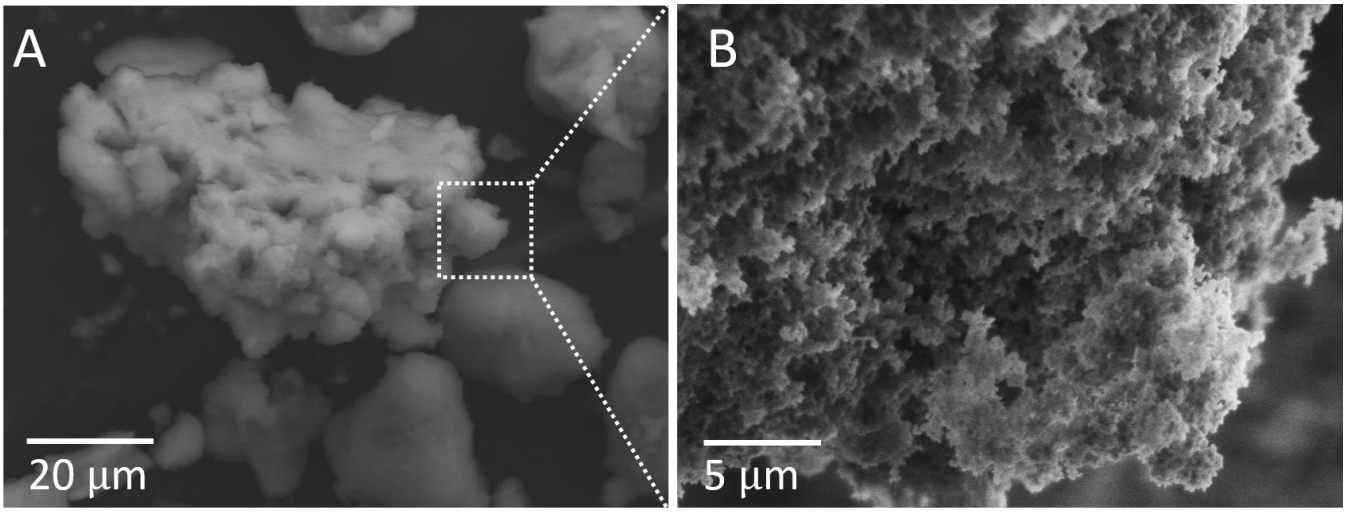

Figure 1. Representative SEM micrographs of (calcined) $Ni_{5\%}SiO_2$ sample displaying (**A**) an overview of a selected silica grain and (**B**) a zooming made on an external layer showing morphological characteristics of the impregnated surface.

Regarding $Ni_{60\%}SiO_2$(Comm), Figure 2A shows that the sample is constituted of bulky silica grains (various dimensions, average diameter around 90 µm) having a rock-like appearance without noticeable cracks or structural defects. The brilliant (light) colors on the white silica surface result from the diffusion of deposited NiO nanoparticles, having higher electronic density than SiO_2, forming independent islands on the external surface. Conversely to $Ni_{5\%}SiO_2$, EDS analyses validate the heterogeneity in Ni-dispersion with some richer Ni-domains than others. Calculated atomic Ni/Si ratios strongly vary from 0.7 to 355, suggesting the presence of zones over which Ni-species manifest in the form of colossal multi-layers. The panoramic image in Figure 2B shows that the species consist of regular octahedra of sizes between 0.5 and 1.0 µm. The magnified image in Figure 2C specifies that side lengths are about 250 nm and the angle between two adjacent edges is equal to 60°. The well-defined octahedral morphology with cubic symmetry could be considered as an indication of cubic-structured NiO crystals (pores are visible on the (111) facet, Figure 2C), as will be evidenced by N_2-sorption data. Additionally, NiO octahedra seem to deposit layer-by-layer, in which the hexagonal and triangular nano-plates appear to have a tendency to preferentially stack along the (111) direction (Figure 2C).

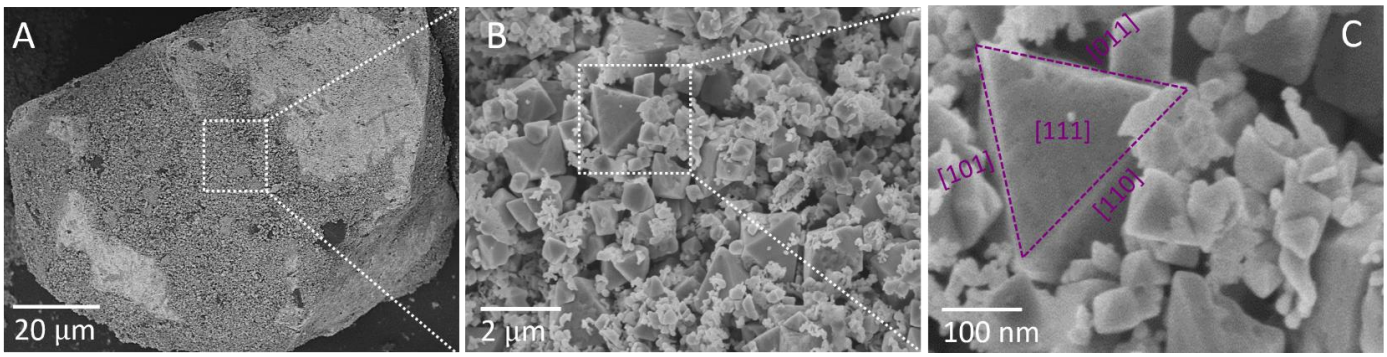

Figure 2. Representative SEM micrographs of (as purchased) $Ni_{60\%}SiO_2$(Comm) sample displaying (**A**) an overall scanning of a silica grain, (**B**) a zooming made on the surface of NiO species covering silica and, (**C**) an enlargement of a typical octahedral particle.

3.2. Reducibility Behaviour and H_2-Uptake Properties of Fresh Samples

Concerning H_2 chemisorption data, TPR profiles of both fresh samples are presented on Figure 3A. The overall experimental H_2-uptake (temperature range: 100–800 °C) estimated from such profiles along with the relative contribution of each peak (determined as a function of consumed hydrogen) are displayed in Table 1. Over both samples, two main types of reducible species can be recognized: (i) those undergoing reduction below 450 °C, attributable to easily reducible or bulk NiO weakly interacting with the support (such as free NiO) and, (ii) Ni species with enhanced interaction with silica, undergoing reduction at higher temperatures, above 450 °C [60]. In correlation with SEM images (Figure 2), the commercial sample is composed of stacked octahedra particles where upper layers are expected to have almost no interaction with the support explaining thus the dominant abundance (around 80% of species, Table 1) of bulk NiO particles undergoing reduction within the 400 °C range. On the other hand, nickel particles over $Ni_{5\%}SiO_2$ are homogeneously distributed (EDS analyses) and thus, higher degree of Ni-SiO_2 interactions (described as Ni-silicate mixed phases) are expected owing to the wider availability of SiO_2 surface sites. Indeed, 66% of impregnated Ni^{2+} ions are reduced (post to calcination) at 540 °C with remaining species being present as free NiO (Table 1). From a catalytic perspective, Ni strongly interacting with the support would result in smaller Ni^0 active centers less prone to deactivation via sintering and consequently more resistant to carbon deposition (discussion based on XRD data and catalysis is introduced below). The overall experimental H_2-uptake at 800 °C (Table 1) for $Ni_{5\%}SiO_2$ is consistent with the complete reduction of the targeted amount of Ni-species (circa 900 μmol g^{-1} for 5 wt% Ni). Remarkably, an additional 21% in H_2-uptake is recorded after complete reduction of $Ni_{60\%}SiO_2$(Comm) (Table 1: experimental uptake of 13,028 μmol g^{-1} for an expected one of circa 10,800 μmol g^{-1} for 60 wt% Ni). This means that NiO species chemisorb the stoichiometric H_2 amount needed for reduction ($NiO + H_2 \leftrightarrow Ni^0 + H_2O$) while storing hydrogen within metallic nickel phases.

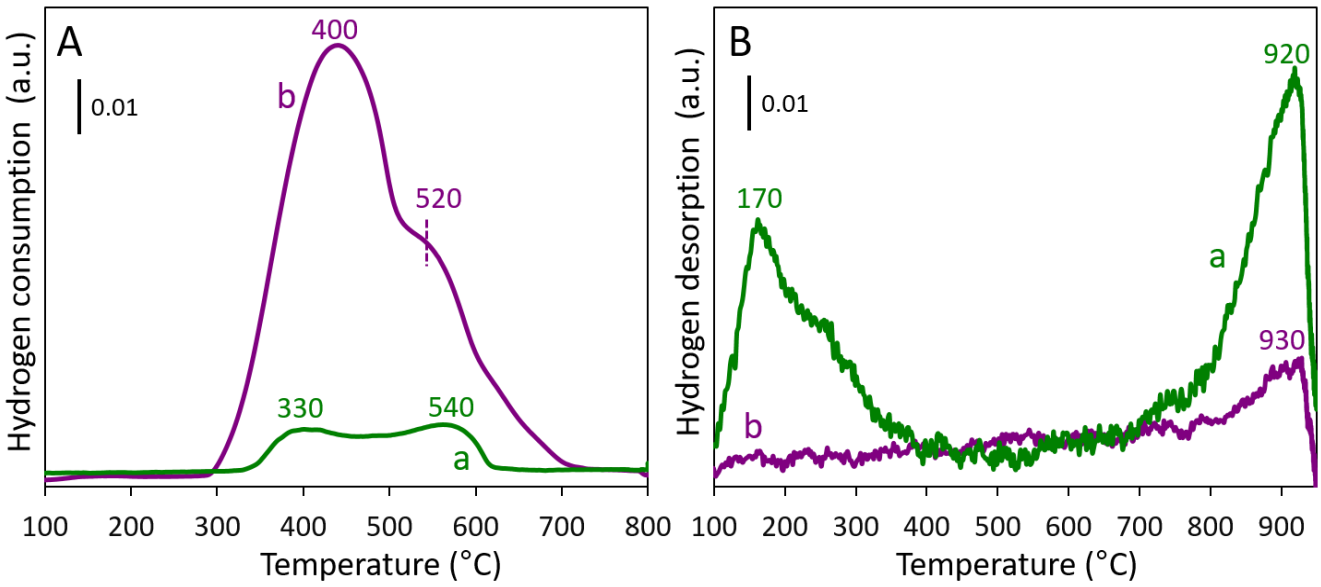

Figure 3. (**A**) H_2-TPR and (**B**) H_2-TPD profiles of silica-based samples: (a) $Ni_{5\%}SiO_2$ and (b) $Ni_{60\%}SiO_2$(Comm).

Table 1. H_2-chemisorption properties of calcined silica-based samples.

Samples	H_2-TPR Analysis			H_2-TPD Analysis
	Peak Temp. (°C)	Relative Contribution (%) [a]	Total H_2-Uptake (μmol g^{-1}) [b]	Dispersion (%) [c]
$Ni_{5\%}SiO_2$	330	34	891	20.9
	540	66		
$Ni_{60\%}SiO_2$(Comm)	400	79	13028	2.7
	520	21		

[a] H_2-uptake associated to each peak relatively to the overall H_2-uptake after complete reduction. [b] H_2-uptake determined experimentally from TPR profiles after complete reduction at T = 900 °C. [c] Ni dispersion calculated based on H_2-TPR and H_2-TPD results.

To validate the hydrogen storage properties of the octahedra Ni-shaped particles, H_2-uptake (over reduced Ni^0 species) followed by H_2-desoption experiments were conducted over both silica-based samples and corresponding profiles and dispersion data are presented on Figure 3B and in Table 1, respectively. Results show that $Ni_{60\%}SiO_2$(Comm) is almost not adsorbing H_2, for the entire temperature range (profile b, Figure 3B), despite its considerable H_2 uptake (followed by MS spectrometry) and Ni content. A weak desorption gas peak appears at elevated temperature possibly attributed to the release of (some) hydrogen retained within the sample during thermal H_2-treatment (after being reduced while subjected to H_2). The relative surface area of this peak is smaller (around 25% in magnitude) than that of the same peak-type detected over $Ni_{5\%}SiO_2$ (profile a, Figure 3B). Such negligible and extremely endothermic H_2-release of Ni species in $Ni_{60\%}SiO_2$(Comm) attest for the high H_2-storage capacity of (originally) structured NiO octahedra, shown to adsorb hydrogen once reduced without releasing it even under favorable desorption conditions. MS signals (data not presented) confirm continuous hydrogen uptake over $Ni_{60\%}SiO_2$(Comm) after reduction (at temperatures above 600 °C, Figure 3A) and during H_2-saturation from 700 °C to room temperature, prior to desorption measurements. For the 5 wt% Ni-containing sample, H_2-desorption comprises two domains of temperature with close relative surfaces (profile b, Figure 3B). Notably, the high temperature peak corresponds to the desorption of H_2 strongly attached to silica, reported to originate from the hydroxylation of pyrogenic silica (as the one used in this study) by reduction of Si^{4+} into Si^{3+} cations and, (ii) the low temperature peak with maxima at 170 °C being linked to the surface desorption of hydrogen from Ni^0 sites [61,62]. Dispersion values (D%, Table 1) accentuate on such differences in desorption behaviors where: a value of only 2.7% is found for $Ni_{60\%}SiO_2$(Comm) compared to 20.9% for $Ni_{5\%}SiO_2$. The dissimilar types of Ni species found in both samples typically: (i) well dispersed Ni^{2+} ions in the case of $Ni_{5\%}SiO_2$ and (ii) nano-structured layered octahedra-based particles in $Ni_{60\%}SiO_2$(Comm), associated with the possible structural changes induced during high temperature H_2-treatment, will affect catalytic properties as well as the amount $C_{(s)}$ deposits after catalysis (as discussed below).

3.3. Catalytic Reactivity in Steam Biogas Reforming

Before catalytic runs, fresh samples were in situ reduced at 650 °C to generate metallic Ni^0 nanoparticles required for the reaction. The in situ reduction temperature was chosen based on H_2-TPR results showing complete reduction of NiO to Ni^0 species, over both silica-based samples, at temperature values not exceeding 550 °C (Figure 3A). The corresponding catalytic performances in terms of reactivity and selectivity as a function of test duration are presented in Figure 4.

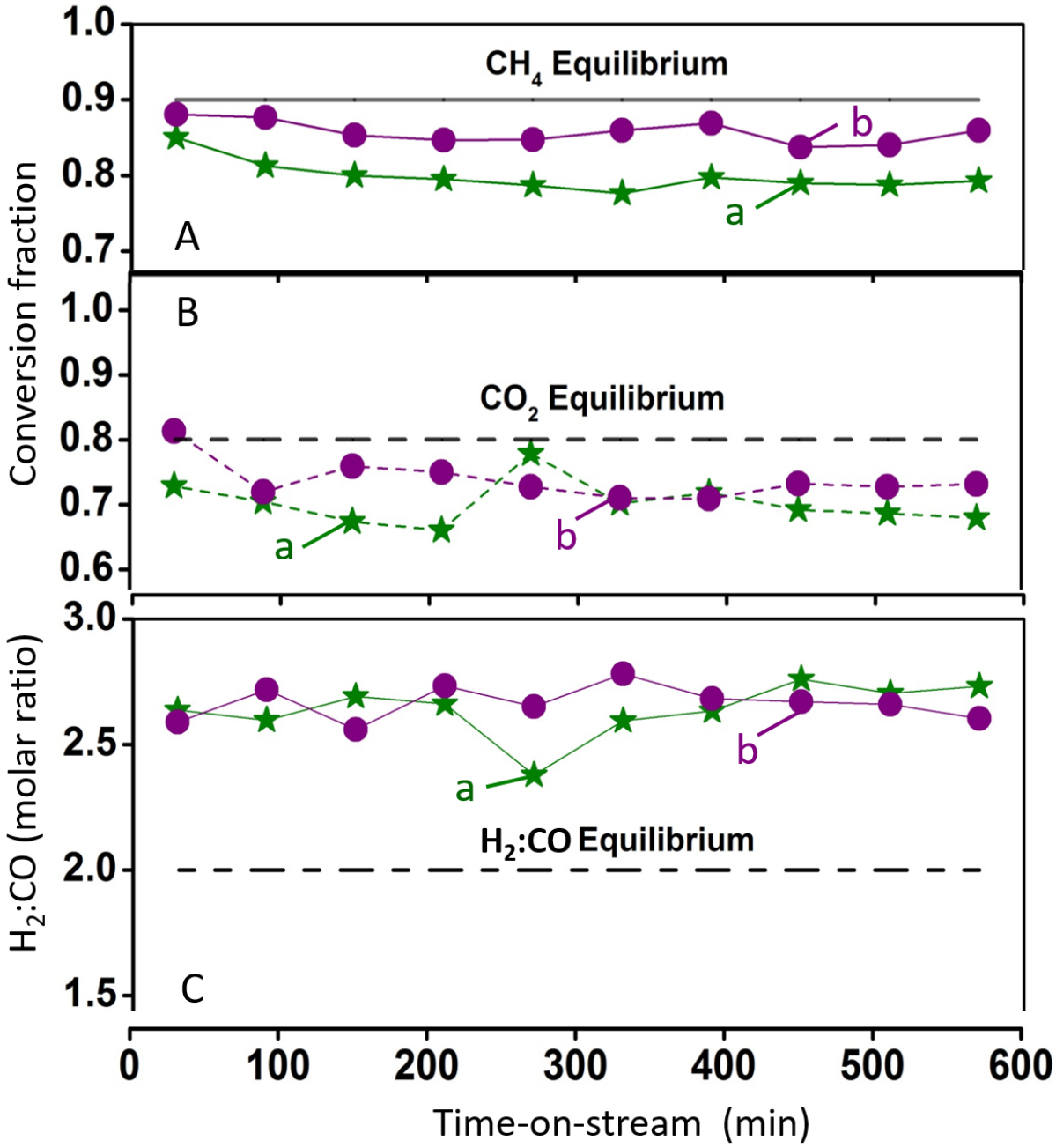

Figure 4. (**A**) CH_4 conversion, (**B**) CO_2 conversion and (**C**) H_2:CO molar product ratio during biogas steam reforming (800 °C/10 h, CH_4:CO_2:H_2O:Ar = 1:0.4:0.8:12, P = 1 atm, GHSV = 67.7 L g_{cat}^{-1} hr^{-1}) as a function of time-on-stream over: (a) $Ni_{5\%}SiO_2$ and (b) $Ni_{60\%}SiO_2$(Comm). Black dashed-lines are thermodynamic values calculated using the HSC 7.1 Chemistry software, for $C_{(s)}$-assisted biogas steam reforming operation.

According to our reaction conditions (CH_4:CO_2 molar ratio of 1:0.4) and based on thermodynamic simulations, a higher CH_4 conversion (by almost 10%) should be expected compared to that of CO_2 (black dashed lines, Figure 4). As a general observation, both silica-based samples are stable with TOS with $Ni_{60\%}SiO_2$(Comm) being more reactive (specifically in terms of methane conversion, Figure 4A) than $Ni_{5\%}SiO_2$ (Figure 4A). This could be associated to the higher nickel content over the commercial sample generating thus a larger number of metallic active centers required for methane activation and subsequent dissociation. The stability of $Ni_{5\%}SiO_2$ under harsh biogas reforming conditions (elevated

temperature and steam-rich medium) is anticipated owing to the physicochemical characteristics of this sample displaying well-dispersed Ni^0 centers (SEM/EDS analyses and H_2-TPD data) of several types, according to their interference in hydrogen adsorption and subsequent desorption (Figure 3B). This potentially generates different types of reactivity sites known to be beneficial for catalysis. Particularly, nickel sites with low temperature H_2-desorption peaks (maxima at 170 °C) are reported to promote the dissociative adsorption of methane on Ni^0 sites ($CH_4 + 2Ni \rightarrow CH\text{-}Ni + H\text{-}Ni$), a step recognized as rate-determining in reforming reactions [63]. The performance of our $Ni_{5\%}SiO_2$ catalyst appears promising and this also stands when compared to literature data obtained by other research teams over supported, mono-or bimetallic, catalysts and even for higher metal loadings. As compared to MgO-supported noble metals (Rh, Ru), methane conversion values were not exceeding 66% over the most performing catalyst (0.5 wt% Ru/MgO) at 900 °C and for a feed molar composition of $CH_4:CO_2:H_2O = 1:0.7:0.3$ [64]. Moreover, for a 10 wt% Ni impregnated over mixed MgO-Al_2O_3 hydrotalcite-like materials promoted with 2.5 wt% CeO_2, CH_4 conversion was around 79% and sample showed deactivation tendencies after 4 h on steam at 700 °C and for an inlet feed composition similar to the one adopted in this study [65]. When alumina was used as catalytic support for Ni (12 wt%) and CeO_2 (6 wt%), both introduced simultaneously via post-impregnation, the resulting catalyst achieved 73% in terms of CH_4 conversion being thus less reactive than our $Ni_{5\%}SiO_2$ sample, for similar reaction conditions [66]. For a Ni (10 wt%)-B_2O_3 (5 wt%) supported over mesoporous SBA-15 catalyst evaluated at 800 °C under a flowing feed of $CH_4:CO_2:H_2O = 1:0.7:0.3$, methane conversion was close to that recorded over $Ni_{5\%}SiO_2$ yet, their sample was bimetallic and richer in nickel [50].

Despite the low dispersion of Ni species over $Ni_{60\%}SiO_2$(Comm) (Table 1) and the larger NiO species (Figure 2) generating eventually bigger Ni^0 nanoparticles (as confirmed from XRD, data discussed below) as compared to $Ni_{5\%}SiO_2$, the commercial catalyst preserved its intrinsic activity levels for 10 h straight. Ordinarily, catalysts reported in literature with such characteristics deactivate steeply on stream via coke deposition and serve as reference materials to highlight on all structural/textural aspects that should be avoided in the design of reactive reforming catalysts [19,25,46]. The notable stable performance could be assigned to the generation of new metallic phases, during in situ reduction, having high hydrogen storage potentials (in line with H_2-TPR/TPD results) and serving as boosters against coke deposition by keeping exposed Ni^0 surfaces clean for catalysis. SEM, TGA/DSC and Raman experiments over the spent catalyst will attest for the high coke resistance of $Ni_{60\%}SiO_2$(Comm).

With respect to selectivity outcomes (Figure 4C), both silica-based samples display H_2:CO molar values higher than the stoichiometric one (around 2.0, black dashed lines). Their selectivity curves present fluctuating trends linked to the fluctuations observed for CO_2 conversion curves (Figure 4B). Furthermore, the difference between CH_4 and CO_2 conversion is exceeding the thermodynamic value of 10% where at particular times, a difference in the range of 25% is noted (i.e., at 210 mints of catalysis over $Ni_{5\%}SiO_2$). Average carbon dioxide conversion is 71% over $Ni_{5\%}SiO_2$ and 73% over the commercial catalyst being lower than the thermodynamic equilibrium value (close to 80%, Figure 2B). High H_2 and low CO yields (responsible for elevated H_2:CO values) indicate the occurrence of H_2-producing reactions and the inhibition of CO-producing ones. In favor of this observation, several possible reactions could interfere in the deviation of the molar H_2:CO composition. A dominant participation of SRM over DRM, owing to the easier activation barriers of H_2O compared to CO_2 [19], favors the excessive production of H_2 via methane activation by water vapor at a higher rate than by carbon dioxide. SRM could be favored over Ni supported on (inert) SiO_2 oxide due to the absence of basic sites within the catalyst composition that interfere in the adsorption of acidic CO_2 molecules [25]. Compared to Al_2O_3 and ZrO_2 oxides, SiO_2 is slightly more acidic than the others (having weak to medium basic adsorption sites) and potentially will not contribute in CO_2 activation as does ZrO_2 [67,68]. An even higher molar ratio of 2.80 has been reported for the same type of

reaction over a core-shell Ni/Al_2O_3 catalyst and authors attributed the low CO selectivity to a decay in the reactions leading to CO formation [69]. The higher CH_4 than CO_2 conversion can be also associated to the occurrence of methane decomposition consuming methane and producing H_2 and carbonaceous deposits. From a thermodynamic perspective, methane decomposition remains favorable at 800 °C (stability temperature) and occurs simultaneously with dry and steam reforming reactions. Coke content and its characterization are discussed below. The non-coke producing RWGS side-reaction (producing CO) is also thermodynamically favorable under our conditions yet in view of the H_2:CO trend; its occurrence seems less probable due to the rise (rather a decline) in H_2:CO ratio. In situ reoxidation of Ni^0 into NiO nanoparticles could have also contributed in lowering CO_2 conversion. In fact, CO_2 is a linear molecule and should bend upon interaction with a surface for dissociation. Carbon dioxide bending preferentially occurs on reduced (O_2-depleted) surfaces rather than on O_2-rich ones [70]. This cause has a minor impact on selectivity in view of the low degree of reoxidation visible on the XRD patterns of spent samples.

In a previous work [45], we found that the introduction of MgO (or CaO) basic modifiers via "one-pot" in the course of alumina precipitation results in $Ni_{5\%}Mg(or\ Ca)_{5\%}Al_2O_3$ catalysts remarkably selective for "metgas" production as compared to catalytically stable and poorly selective $Ni_{10\%}Al_2O_3$ catalyst. Even though silica-based catalysts are stable for this reaction, their selectivity should be further enhanced by addition of phases that could greatly favor CO_2 adsorption (i.e., MgO, La_2O_3 or CaO). In this pilot study, the non-addition of a basic element is intentional since our aim is to highlight on the unique hydrogen storage properties of octahedra-based Ni species on coke formation and accumulation.

3.4. Study of Carbon Deposition and Morphological Aspects of Spent Catalysts

TGA coupled to DSC experiments, Raman spectroscopy and SEM were conducted to study and quantify carbonaceous deposits over spent SBR silica-based catalysts.

Combined TGA and DSC measures (Figure 5A,B) were carried out in an oxidative medium (air), in a temperature range between 250 and 900 °C, to recognize the type and amount of deposited $C_{(s)}$-species based on their oxidation temperatures (mainly sp^2 (grapheme, nanotubes) and sp^3 (graphite) carbon types) and overall decrease in sample weight, respectively [71,72]. The primary significant comment provided by TGA is the $C_{(s)}$ content over spent catalysts that is almost negligible over $Ni_{60\%}SiO_2$(Comm) whereas an amount of 11 wt% is found over (catalytically stable) $Ni_{5\%}SiO_2$ (Figure 5A). Such result found over $Ni_{5\%}SiO_2$ is in complete accordance with the previously elaborated hypothesis regarding selectivity data. Indeed, the high H_2:CO molar ratio exceeding thermodynamic value is originating from MD reaction yielding considerable $C_{(s)}$ amounts along with hydrogen. Concerning DSC profiles (Figure 5B), exothermic peaks reveal two main types of carbonaceous species described as (i) Cβ (C-nanotubes, peak 450–550 °C) and (ii) Cγ (graphite, peak 550–750 °C) [71]. The presence of crystalline Cγ graphitic carbon in this sample is critical since an accumulation of this type is crucial towards reactivity due to its high thermal stability (extensive energy requirement for regeneration) and its encapsulation of active metallic sites [72]. Due to the pre-dominance of high temperature DSC signal, it is alluring to deduce that carbon in spent $Ni_{5\%}SiO_2$ manifests (mainly) as Cγ graphite. In view of the stable performance of $Ni_{5\%}SiO_2$ (profiles a, Figure 4), such carbonaceous deposits are not affecting reactivity due to one (or more) of the following reasons: (i) they could correspond to less toxic transitory intermediate carbon species formed during gradual in situ transformation of reactive Cα and/or Cβ into Cγ, or (ii) they are present in low amounts (as evidenced by XRD, Raman and SEM data) or (iii) despite the deposition of Cγ, numerous Ni^0 sites are still accessible for catalysis while others are encapsulated by graphite. Nevertheless, if $Ni_{5\%}SiO_2$ is allowed to operate for longer runs, more carbon (perhaps mature graphite) will eventually deposit and its accumulation will become detrimental towards the reactor (potential blockage and increase in pressure) as well as catalysis. As anticipated, DSC peaks are almost absent over spent $Ni_{60\%}SiO_2$(Comm) (curve b,

Figure 5B), in line with the very small $C_{(s)}$ content. In correlation with selectivity, the possible deviation of H_2:CO ratio away from "metgas" could also be the result of in situ H_2 production by MD without detectable carbon deposition/accumulation. Hydrogen molecules stored within Ni^0 layers (during in situ reduction) are at the origin of the high-coke resistance of $Ni_{60\%}SiO_2$(Comm) as they provide a hydrogenation medium (or an in situ regeneration path) for carbon as soon as it deposits ($C_{(s)} + 2H_2 \leftrightarrow CH_4$). Moreover, it is worth noting that the reaction of $C_{(s)}$ with H_2 is thermodynamically favorable at the chosen stability temperature of 800 °C [19]. Although methane, a reactant, can be in situ generated, its amount remains significantly smaller than its inlet content. Basically, the occurrence of the coke gasification reaction into methane gas will not lead to a shift in thermodynamics towards formation of reactants.

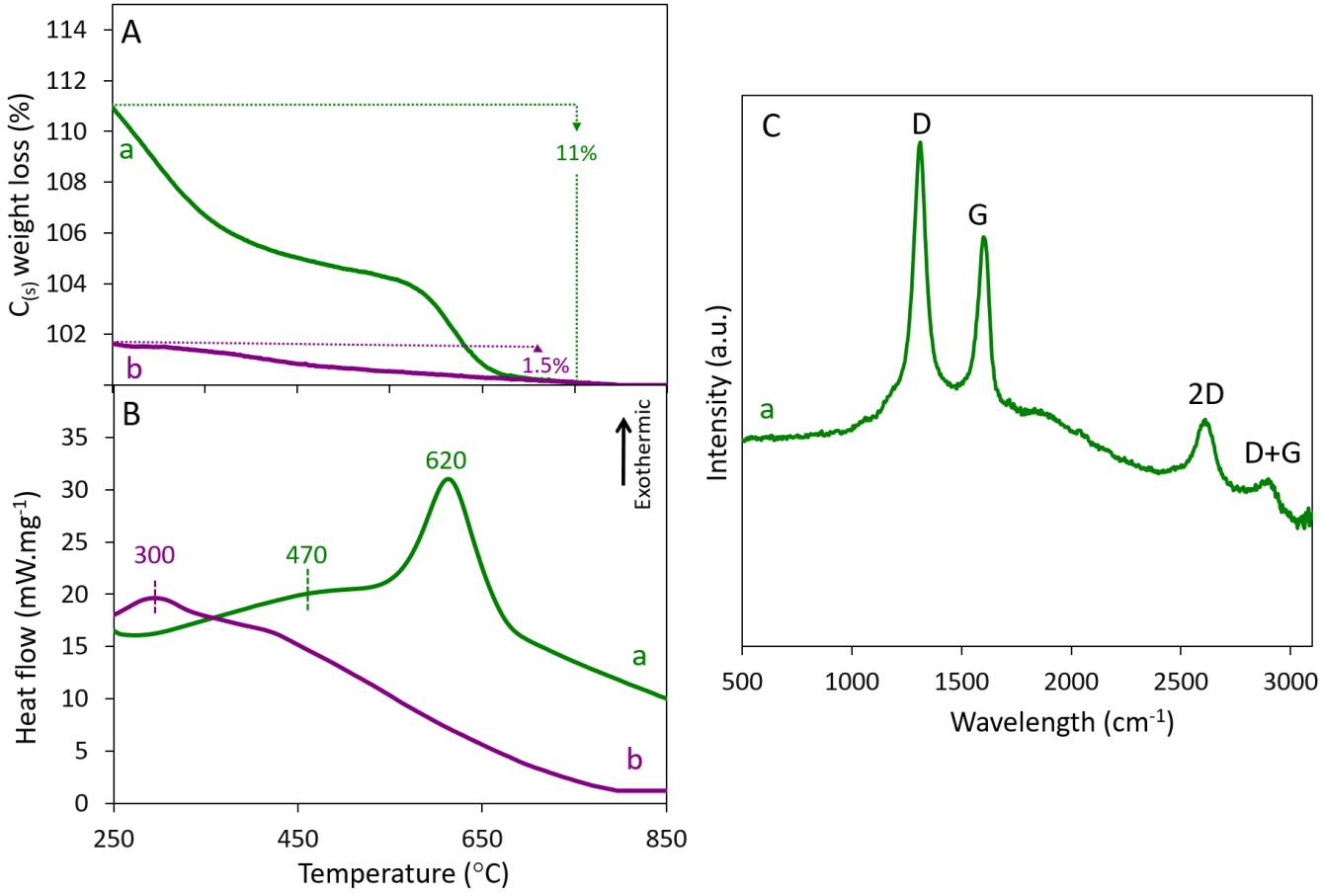

Figure 5. (**A**) TGA, (**B**) DSC profiles and (**C**) Raman spectrum of spent (800 °C/10 h, CH_4:CO_2:H_2O:Ar = 1:0.4:0.8:12, P = 1 atm, GHSV = 67.7 L g_{cat}^{-1} hr^{-1}) catalysts: (a) $Ni_{5\%}SiO_2$ and (b) $Ni_{60\%}SiO_2$(Comm).

Complementary to TGA/DSC, Raman signals were only obtained for the spent $C_{(s)}$-richer $Ni_{5\%}SiO_2$ (Figure 5C) where spent $Ni_{60\%}SiO_2$(Comm) catalyst, with trivial amounts of coke, presented a strong fluorescence background that hampered correct data detection. The bands in the spectrum of spent $Ni_{5\%}SiO_2$ are standard of doubly degenerated phonon mode of C atoms in sp^2 networks characterized by a high degree of symmetry (graphitic carbon, G-band, 1601 cm^{-1}) and of disordered structural mode of carbon species (D-band, 1312 cm^{-1}) [73,74]. The signal strength of D-band compared to G-band (expressed as intensity ratio I_D/I_G) is a useful parameter for indicating the degree of crystallinity and/or the existence of structural defects within carbon species. The higher the ratio (value above one), the lower the structural order is within carbonaceous deposits. The calculated I_D/I_G ratio for spent $Ni_{5\%}SiO_2$ is 1.19, being slightly higher than unity, supporting (to some

extent) the supposition of the disordered (rather than well-ordered graphite) character of the formed carbon. Additionally, the occurrence of Raman peaks at circa 2700 and 2900 cm^{-1} (indexed as D and (D + G) bands, respectively, Figure 5C) are typical reflections of scattered carbonaceous species with poorly crystalline structures [45]. This is in turn an evidence of the presence of disorder and/or of defects in sp^2 coke networks.

The differences noticed on the level of coke handling (deposition/accumulation or in situ regeneration) over both silica-based catalysts are furthermore highlighted by considering the morphological aspects of spent catalysts by SEM (Figure 6). For spent $Ni_{5\%}SiO_2$, silica grains preserved their original spongy-like exterior with no apparent structural modification after 10 h of catalysis at 800 °C and in presence of steam (Figure 6A). The calculated Ni/Si atomic ratios were in the range of 0.057 and 0.066 being slightly higher than the values obtained over the fresh sample (Section 3.1). Some Ni^0 particles have sintered during catalysis (as evidenced from XRD data, discussed below) which initiated carbon deposition on the external surface of the catalyst (Figure 6A'). In this sample, small $C_{(s)}$-domains recognized by irregular short-carbon filaments are assembled on particular locations where some silica zones appear more covered than others. SEM examination of these deposits in accordance with available literature [75–77] reveal that such carbon nanocoils are neither standard nanotubes will well-defined "bamboo" shapes nor pure graphitic deposits with tubular or closed inner layers but rather an intermediate carbon phase having common properties from each carbonaceous family (as discussed previously based on TGA/DSC and Raman data). Here again, the peculiar character of carbon over $Ni_{5\%}SiO_2$ is put into evidence justifying the stable reactivity profile despite coke accumulation. On the other hand, the external surface of $Ni_{60\%}SiO_2$(Comm) is free of carbonaceous deposits (Figure 6B) and when compared to the morphology before catalysis (Figure 2A), surface is more exposed and appears as a smooth glassy like-exterior (Figure 6B). The previously identified Ni octahedra shapes (Figure 2B,C) are no longer present rather, nanoparticles with lamellar crystalline junctions are observed (Figure 6B'). Calculated Ni/Si atomic ratios vary between 0.4 and 410 dictating an uneven distribution of Ni over silica, an observation also valid for the case of the fresh sample (Section 3.1). We tentatively associate the "trellis" shape of metallic nano-species to an annealing effect induced during in situ reduction for transformation of oxides into metallic active (for catalysis) sites. We presume that nanoparticles will sharply grow by fusing with neighboring nanoparticles, after phase nucleation, whilst subjected to an endothermic forced chemical transformation (reduction under excess H_2 stream) causing the disappearance of the structured shape and the formation of quasi-spherical particles. It has been stated that H_2-annealing heat treatments can easily transform structured oxides into metals yet, such processes are usually accompanied by significant changes in the original morphology [3]. Actually, such physical transformation of shapes has been reported in the recent literature for urchin-like α-Fe_2O_3 and Fe_3O_4 nanostructures when studied under various H_2-reduction media [78]. It was found that upon treating structured iron species at temperatures higher than 650 °C and in presence of hydrogen, the original urchin shape is completely lost and nanorods of metallic Fe^0 species are generated. With respect to our H_2-TPD results regarding hydrogen storage of annealed Ni^0 nanorods, such a property is rarely studied in literature for materials that underwent changes under H_2-treatments. This is mainly associated to the fact that H_2-annealed materials are normally considered for their high microwave-absorbing potentials and electromagnetic resistances [3,78]. Their usage for SBR, while characterized at different stages, result in their consideration as remarkably resistant anti-coking reforming catalysts.

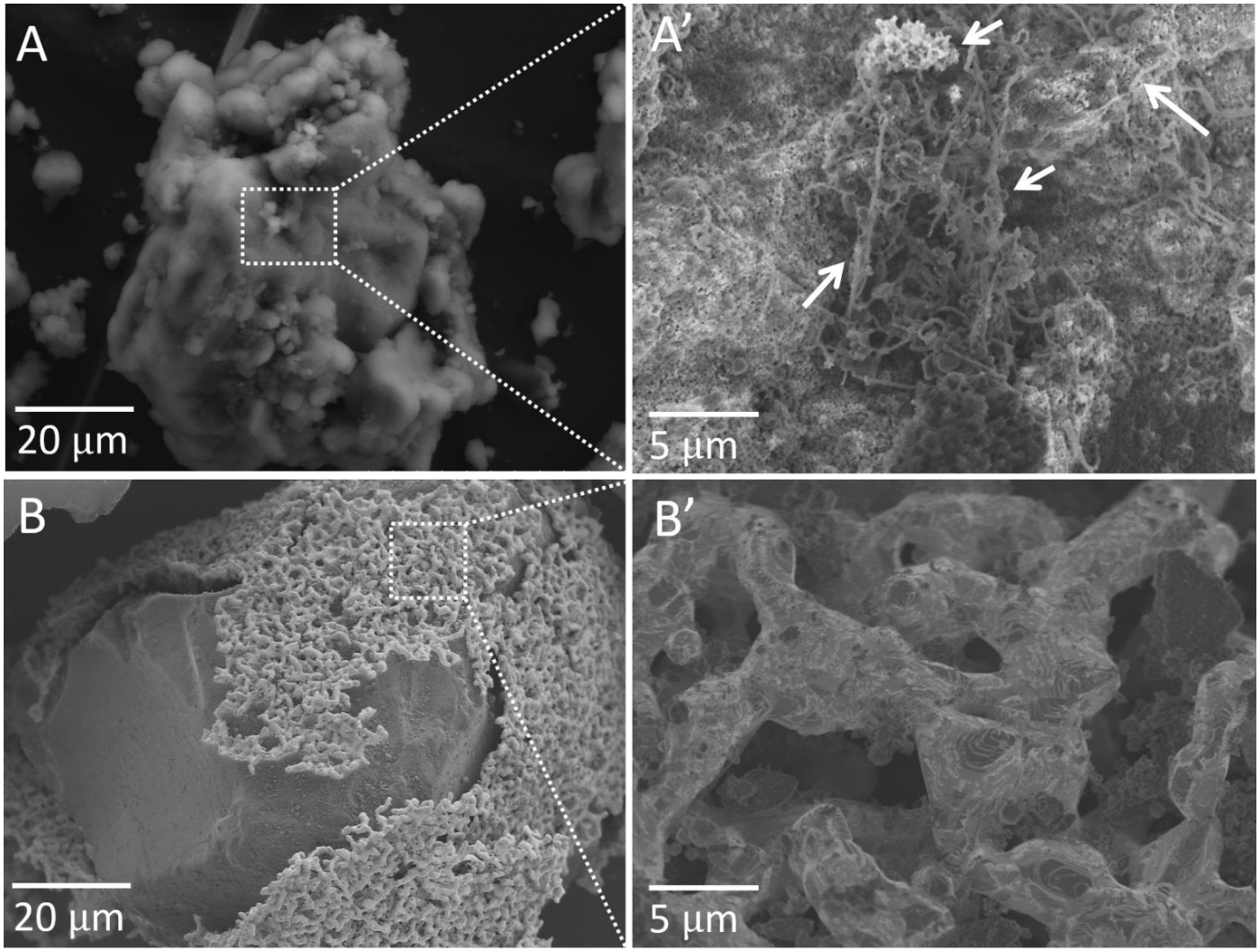

Figure 6. SEM micrographs of spent (800 °C/10 h, CH_4:CO_2:H_2O:Ar = 1:0.4:0.8:12, P = 1 atm, GHSV = 67.7 L g_{cat}^{-1} hr^{-1}) (**A**,**A'**) $Ni_{5\%}SiO_2$ and (**B**,**B'**) $Ni_{60\%}SiO_2$(Comm) catalysts. Some carbon deposits are marked with arrows.

3.5. Structural and Textural Properties of Silica-Based Catalysts

Dispersion and state of nickel species in fresh, in situ H_2-reduced and spent $Ni_{5\%}SiO_2$ and $Ni_{60\%}SiO_2$(Comm) catalysts are confirmed by XRD (patterns plotted on Figure 7A and 7B, respectively) and corresponding average particle size determined from diffractograms (at the various stages) are stated in Table 2. The higher amount and consequently the poor dispersion of nickel over the commercial catalyst resulted in much sharper diffraction peaks for NiO and Ni^0 (Figure 7B) compared to same peak positions over $Ni_{5\%}SiO_2$ (Figure 7A). In line with SEM/EDS observations, octahedra-shaped NiO nanoparticles, with face centered cubic (FCC) unit cell (ICDD file # 089-7130), present larger dimension of coherent domain sizes than NiO dispersed over Aerosil (FCC unit cell, ICDD file # 089-7130) generating thus bigger Ni^0 species (FCC unit cell, ICDD file # 65-0380) during H_2-reduction and after catalysis (Figure 7A,B and Table 2). Compared to diffraction patterns of $Ni_{60\%}SiO_2$(Comm), those of $Ni_{5\%}SiO_2$ present an additional broad signal at about 22° (Figure 7A), characteristic of diffusion of X-ray into amorphous silica walls. The absence (or non detection) of this peak over the commercial sample results from the high coverage of silica surafce by nickel species. On the other hand, the diffraction patterns of spent SBR catalysts (profiles a" and b", Figure 7A,B) reveal the presence of both Ni^0 (active phase) and NiO crystalline phases. Such partial nickel reoxidation (in a steam-rich medium) on both silica-based catalysts having distinct Ni dispersion shows that reoxidation is not size

dependent (Table 2). Rather, it occurs preferentially over silica than on other oxides (i.e., alumina), an interpretation noted from our recent study [46]. As mentioned in Section 3.3, reoxidation had no significant impact on catalysis owing to stable CH_4 and CO_2 conversion levels (Figure 4A,B). A comparison of Ni^0 sizes before and after catalysis shows that some sintering (or thermal agglomeration) took place over the Aerosil-based sample (Table 2). Sintering of nanoparticles is favored at high reaction temperatures especially when conducted in presence of steam [79]. Agglomerated Ni^0 species become then eligible to carbon formation explaining thus the amount of carbonaceous deposits identified by TGA analysis (Section 3.4). The absence of a mesoporous structure, of an anti-coking element (i.e., CaO, CeO_2, MgO) and/or of a specific tactic for enhancement of sintering resistance will eventually lead to coke deposition/accumulation. For $Ni_{60\%}SiO_2$(Comm), XRD data (Table 2) show that Ni^0 chains did not sinter under stream despite harsh reaction conditions. Annealed species could be then considered as rigid assembly of nanoparticles housing hydrogen molecules that act as active in situ regeneration centers for gasification of carbon deposits. Despite the large size of Ni^0 species (Table 2) and their layered configuration (Figure 6B′), diffusional limitations of stored H_2 could occur however, the absence of solid $C_{(s)}$ deposits indicates that limitations are narrowed and that hydrogen can continuously diffuse through metallic layers at 800 °C.

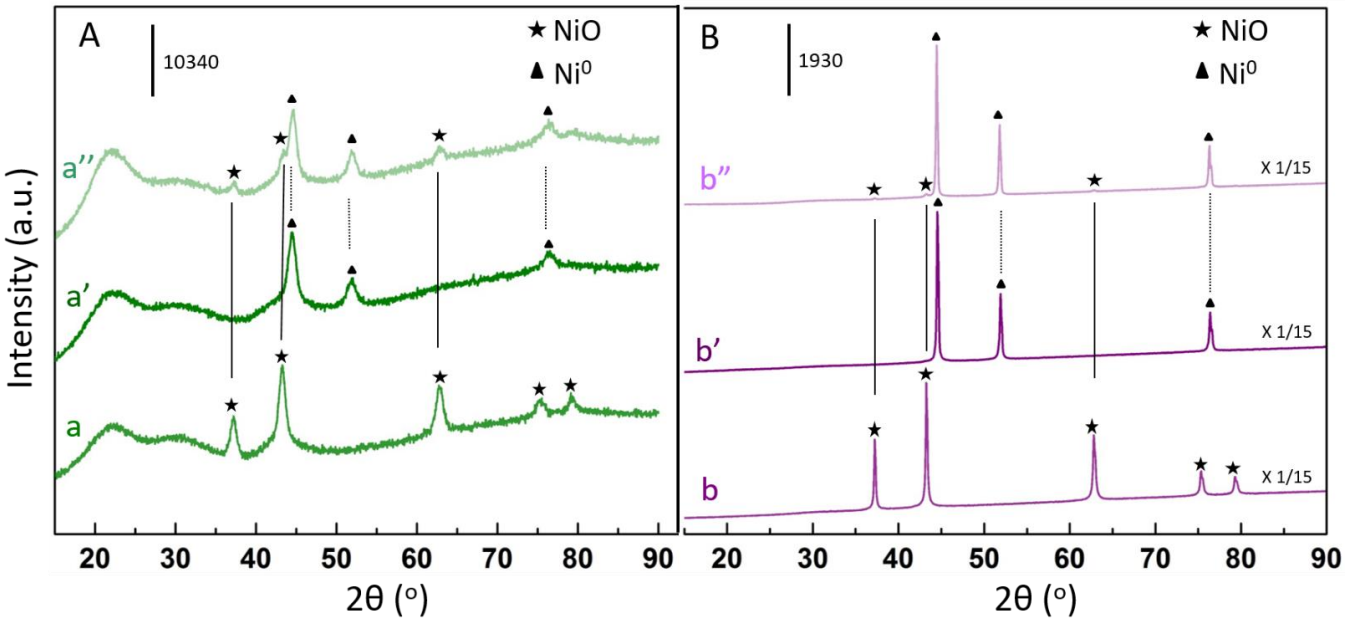

Figure 7. XRD patterns of (**A**) $NiSiO_2$ (a: fresh, a′: in situ H_2-reduced and a′′: spent) and (**B**) $Ni_{60\%}SiO_2$(Comm) (a: fresh, a′: in situ H_2-reduced and a′′: spent) catalysts.

Table 2. Average particle size of nickel species in calcined [a], in situ H_2-reduced (650 °C/2 h) [b] and spent [a,b] (800 °C/10 h, CH_4:CO_2:H_2O:Ar = 1:0.4:0.8:12, GHSV = 67.7 L g_{cat}^{-1} h^{-1}) silica-based catalysts.

Samples	Calcined, Ø (nm)	In Situ Reduced, Ø (nm)	Spent, Ø (nm)	
	NiO	Ni^0	NiO	Ni^0
$Ni_{5\%}SiO_2$	9.7	7.4	4.5	9.8
$Ni_{60\%}SiO_2$(Comm)	44	40	4.3	40.6

[a] Calculated using Scherrer's equation at 2Θ = 62.6° for the [220] indexed plane. [b] Calculated using Scherrer's equation at 2Θ = 51.8° for the [220] indexed plane.

In order to check for any textural change that might be induced in the course of catalysis and to understand the impacts of annealing on porosity and available porous volume; N_2-sorption experiments were performed over fresh and spent samples (isotherms

shown on Figure 8) and corresponding data are listed in Table 3. For the Aerosil-based catalyst (curves a and a', Figure 8), the sharp increase in the quantity of adsorbed N_2 near the high relative pressure range (P/P_0 between 0.7 and 0.95) indicates an uptake of gaseous nitrogen by large pores resulting in considerable porous volumes (Table 3). Their wide PSD (inset figure) is typical of non-ordered macroporous systems where porosity is generated from void spaces between silica grains (inter-granular porosity). Compared to its calcined form, spent $Ni_{5\%}SiO_2$ exhibits relatively smaller specific surface area (Table 3), mainly due thermal contraction and/or condensation by dehydration and dehydroxylation of SiO_2 during high temperature reaction. Moreover, thermal agglomeration with consecutive plugging access of N_2 towards external available surface (or voids between grains) is perhaps a reason for reduction of surface area after catalysis. On the other hand, despite the octahedral morphology destruction over $Ni_{60\%}SiO_2$(Comm), spent catalyst preserved its original textural properties (Table 3) and its isotherm shape (curves b and b', Figure 8). PSD (inset figure) of the fresh and the spent catalyst are sharp and uniformly located within the conventional range of mesopores with N_2-sorption analysis demonstrating typical type IV isotherms with H_1-type hysteresis loops, reflected by the appearance of capillary condensation steps at P/P_0 = 0.6–0.8 [46]. The original nickel octahedra nanoparticles have an ordered mesoporous network that remains fully accessible for gases (i.e., nitrogen) after thermally annealed into nanorods of Ni^0 species and even after being exposed to reaction medium for 10 h straight. This is in consensus with catalysis where: CH_4, CO_2 and H_2O gases can continuously flow within porous Ni^0 layers without facing textural blockage justifying the stable reactivity trend (Figure 4). Based on N_2-sorption data, the annealing effect is viewed as a physical shape-associated transformation rather than a melting mechanism, a term frequently adopted in literature to describe structured nanoparticles submitted to hydrogen annealing heat treatments [3,78]. In such reported studies, H_2-induced heat treatments result in an annihilation of texture accompanied by a massive shrinkage in porosity. Herein, we can describe the obtained annealing process in terms of a three-step mechanism: (1) diffusion of H_2 towards reactive centers and adsorption on the surface, (2) reaction between adsorbed H_2 and NiO yielding metallic Ni atoms and H_2O and, (3) nucleation of Ni atoms to form metallic nanorods while simultaneously storing H_2 molecules.

Table 3. Textural properties of calcined and spent silica-based samples.

Samples	Metal Weight % [a]	BET Surface Area ($m^2\ g^{-1}$)		Pore Volume ($m^3\ g^{-1}$)		Average Pore Diameter (nm) [d]	
		calc. [b]	spt. [c]	calc. [b]	spt. [c]	calc. [b]	spt. [c]
$Ni_{5\%}SiO_2$	4.7	245	140	0.56	0.55	n.d.	n.d.
$Ni_{60\%}SiO_2$(Comm)	60	143	128	0.28	0.27	8±7	7 ±5

[a] Results based on elemental chemical analysis performed on fresh (calcined) samples. [b] Textural values of calcined (in air) samples (450 °C/5 h for $Ni_{5\%}SiO_2$; 300 °C/7 h for $Ni_{60\%}SiO_2$(Comm), commercially treated). [c] Textural values of spent catalysts (800 °C/ 10 h, CH_4:CO_2:H_2O:Ar = 1:0.4:0.8:12, P = 1 atm, GHSV = 67.7 L $g_{cat}^{-1}\ h^{-1}$). [d] Average pore diameter ± standard deviation from the maxima. n.d. not determined owing to the absence of a well-defined peak in the pore size distribution profile.

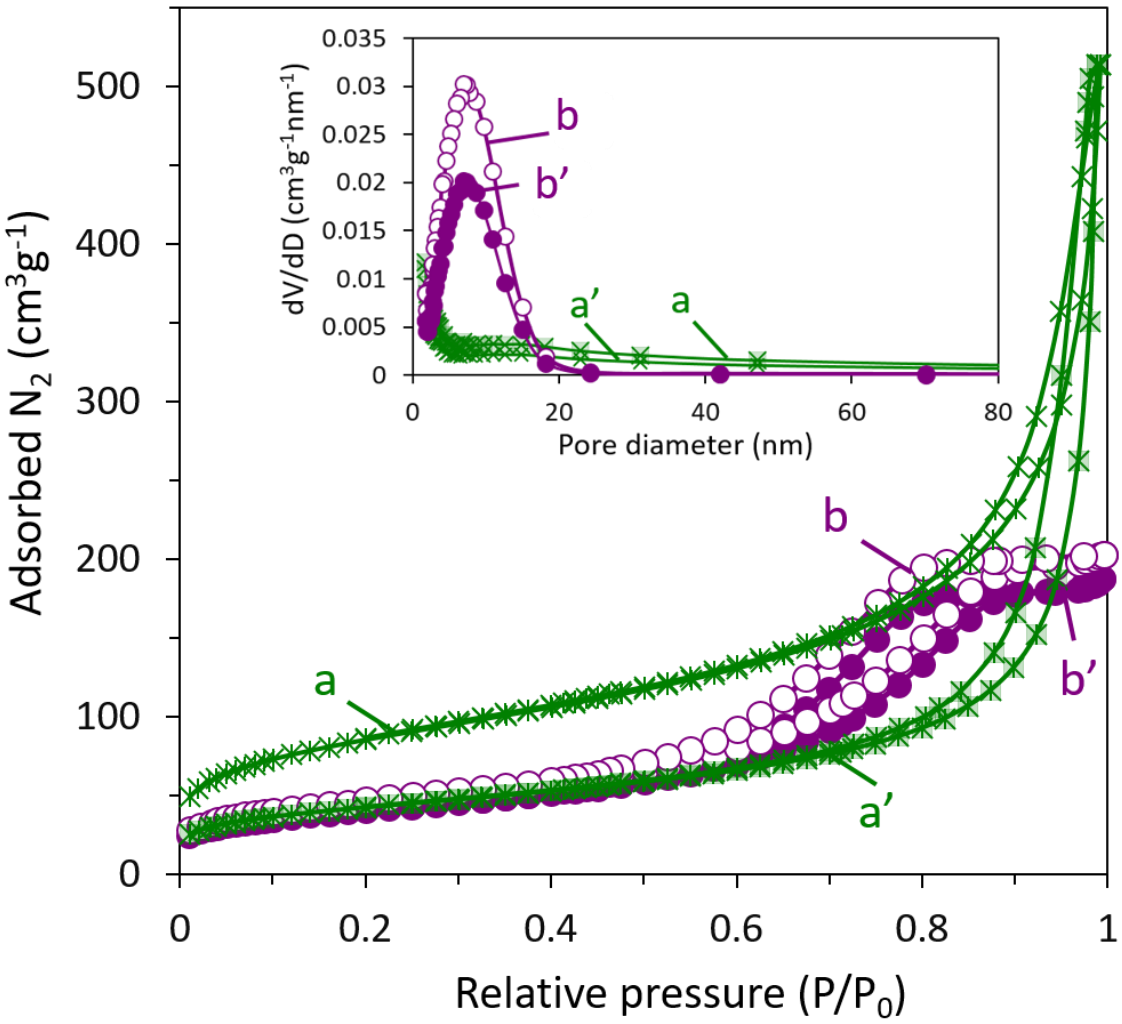

Figure 8. N_2-sorption isotherms along with pore size distributions (insets) of (green curves) $Ni_{5\%}SiO_2$ (a: fresh and a': spent) and (purple curves) $Ni_{60\%}SiO_2$(Comm) (a: fresh and a': spent) catalysts.

4. Conclusions

The aim of this work was to characterize, evaluate and understand the effect of using an originally structured NiO octahedra nanoparticles supported on silica surface as a novel catalyst for syngas generation by means of steam biogas reforming. The $Ni_{60\%}SiO_2$(Comm) catalyst presented stable catalytic performance on stream with conversion levels being close to expected thermodynamic values and to those obtained over a reference $Ni_{5\%}SiO_2$ catalyst, prepared by adopting the "two solvents" post-impregnation method. Average CH_4 and CO_2 conversion values were equal to 85 and 73% over $Ni_{60\%}SiO_2$(Comm) and 80 and 71% over $Ni_{5\%}SiO_2$, respectively. The enhanced reactivity was mainly ascribed to higher Ni content over the structured sample providing wider active sites for catalysis. Despite stable performance, monometallic silica-based catalysts presented poor selectivity towards "metgas" (H_2:CO close to 2.0) associated to several reasons including methane decomposition leading to H_2 and $C_{(s)}$ productions and accounting for the elevated selectivity outcome values. Indeed, considerable amounts of carbon deposits (11 wt%, partially graphic types) were identified over $Ni_{5\%}SiO_2$ whereas, a high resistance to $C_{(s)}$ accumulation was noted over $Ni_{60\%}SiO_2$(Comm) with an oxidative loss of only 1.5% of its weight after 10 h of catalysis.

It was found that different families of Ni species were recognized over both catalysts where each family induced particular physicochemical characteristics that lead to distinct

behaviors with respect to shape preservation, textural aspects and coke handling during catalysis. An annealing effect of mesoporous NiO octahedra, in the course of reduction of $Ni_{60\%}SiO_2$(Comm), resulted in the formation of metallic grids (with no particular geometric configuration) that remained mesoporous even after stability evaluation at 800 °C. The amount of H_2-upatke required for the chemical conversion of octahedra NiO into trellis of Ni^0 nanoparticles exceeded the theoretical value by 21%, attesting for H_2-storage within layered Ni^0 assemblies. Excess hydrogen was shown to be retained within Ni^0 nanorods with negligible desorption potentials; an observation scarcely reported in literature over H_2-annealed nanoparticles. Such a property was found remarkably beneficial for coke minimization during catalysis. Hydrogen molecules acted as barriers against carbon accumulation by providing accessible in situ regeneration centers for coke gasification. Several attempts are reported in the current literature for increasing coke resistance of reforming catalysts. The application of octahedra-based NiO particles can be considered as an additional tactic that is less-time consuming, efficient, does not require expensive metal addition (i.e., noble metals) neither extensive pre-nor post-catalytic treatments. Treating the sample under hydrogen prior to catalysis, a standard preparation step for generation of Ni^0 active sites, is the sole requirement for attaining stable performances (even under harsh reaction conditions) with low carbon deposition for long TOS runs. In light of their textural, structural and catalytic performances, octahedra-based NiO nanoparticles are believed to have a wide-range of applications in renewable energy production, waste to energy conversion and, consequently in gas to liquid (GTL) processes.

Acknowledgments: The authors sincerely acknowledge financial support from the "Agence Universitaire de la Francophonie" (AUF) and the Research Council of the University of Balamand through BIRG 14/2012 and 01/2013 internal funds. The authors are also sincerely grateful to the French-Lebanese CEDRE Hubert Curien program (PHC) for financial support to mobility (project number 30962ZH, 2014-2015). Moreover, authors are grateful to the ERANET EU-FP7 initiative, the national ANR (France) and CNRS-L (Lebanon) agencies for their financial support through the SOL-CARE (Energy-065, 2016-2019) project (JC-ENERGY-2014 first call). The authors would like to thank Ms. Sandra Casale for SEM observations and Dr. Jean-Marc Krafft for his help in setting Raman instrumentation.

References

1. Mou, F.Z.; Guan, J.G.; Xiao, Z.D.; Sun, Z.G.; Shi, W.D.; Fan, X.-A. Solvent-mediated synthesis of magnetic Fe_2O_3 chestnut-like amorphous-core/γ-phase-shell hierarchical nanostructures with strong As (v) removal capability. *J. Mater. Chem.* **2011**, *21*, 5414–5421.
2. Gottschalk, F.; Sun, T.; Nowack, B. Environmental concentrations of engineered nanomaterials: Review of modeling and analytical studies. *Environ. Pollut.* **2013**, *181*, 287–300.
3. Tong, G.; Hu, Q.; Wu, W.; Li, W.; Qian, H.; Liang, Y. Submicrometer-sized NiO octahedra: Facile one-pot solid synthesis, formation mechanism, and chemical conversion into Ni octahedra with excellent microwave-absorbing properties. *J. Mater. Chem.* **2012**, *22*, 17494–17504.
4. Guisbiers, G.; Buchaillot, L. Modeling the melting enthalpy of nanomaterials. *J. Phys. Chem.* **2009**, *113*, 3566–3568.
5. Narayanan, R.; El-Sayed, M.A. Catalysis with transition metal nanoparticles in colloidal solution: Nanoparticle shape dependence and stability. *J. Phys. Chem. B* **2005**, *109*, 12663–12676.
6. Zecchina, A.; Groppo, E.; Bordiga, S. Selective catalysis and nanoscience: An inseparable pair. *Chem. Eur. J.* **2007**, *13*, 2440–2460.
7. Wang, Y.; Sun, T.; Yang, D.; Liu, H.; Zhang, H.; Yao, X.; Zhao, H. Structure, reactivity, photoactivity and stability of Ti-O based materials: A theoretical comparison. *Phys. Chem. Chem. Phys.* **2012**, *14*, 2333–2338.
8. Zheng, S.J.; Wang, Y.G.; Zhang, B.; Zhu, Y.L.; Liu, C.; Hu, P.; Ma, X.L. Identification of $MnCr_2O_4$ nano-octahedron in catalyzing pitting corrosion of austenitic stainless steel. *Acta Mater.* **2010**, *58*, 5070–5085.
9. Wu, J.; Zhang, J.; Peng, Z.; Yang, S.; Wagner, F.T.; Yang, H. Truncated octahedral Pt_3Ni oxygen reduction reaction electrocatalysts. *J. Am. Chem. Soc.* **2010**, *132*, 4984–4985.
10. Cheng, Y.; Zheng, Y.; Wang, Y.; Bao, F.; Qin, Y. Synthesis and magnetic properties of nickel ferrite nano-octahedra. *J. Solid State Chem.* **2005**, *178*, 2394–2397.
11. Bhowmick, I.; Roehl, A.J.; Neilson, J.R.; Rappé, A.K.; Shores, M.P. Slow magnetic relaxation in octahedral low-spin Ni (III) complexes. *Chem. Sci.* **2018**, *9*, 6564–6571.
12. Dorazio, S.J.; Olatunde, A.O.; Tsitovich, P.B.; Morrow, J.R. Comparison of divalent transition metal ion paraCEST MRI contrast agents. *J. Biol. Inorg. Chem.* **2014**, *19*, 191–205.

13. Liu, J.; Cao, M.-S.; Luo, Q.; Shi, H.-L.; Wang, W.-Z.; Yuan, J. Electromagnetic property and tunable microwave absorption of 3D nets from nickel chains at elevated temperature. *ACS Appl. Mater. Interfaces* **2016**, *8*, 22615–22622.
14. Sulaiman, J.E.; Zhu, S.; Xing, Z.; Chang, Q.; Shao, M. Pt-Ni octahedra as electrocatalysts for the ethanol electro-oxidation reaction. *ACS Catal.* **2017**, *7*, 5134–5141.
15. Kong, F.; Ren, Z.; Banis, M.N.; Du, L.; Zhou, X.; Chen, G.; Zhang, L.; Li, J.; Wang, S.; Li, M.; et al. Active and stable Pt-Ni alloy octahedra catalyst for oxygen reduction via near-surface atomical engineering. *ACS Catal.* **2020**, *10*, 4205–4214.
16. Schiaroli, N.; Lucarelli, C.; de Luna, G.S.; Fornasari, G.; Vaccari, A. Ni-based catalysts to produce synthesis gas by combined reforming of clean biogas. *Appl. Catal. Gen.* **2019**, *582*, 117087.
17. Pakhare, D.; Spivey, J. A review of dry (CO_2) reforming of methane over noble metal catalysts. *Chem. Soc. Rev.* **2014**, *43*, 7813–7837.
18. Gao, Y.; Jiang, J.; Meng, Y.; Yan, F.; Aihemaiti, A. A review of recent developments in hydrogen production via biogas dry reforming. *Energ. Convers. Manage.* **2018**, *171*, 133–155.
19. Jabbour, K. Tuning combined steam and dry reforming of methane for "metgas" production: A thermodynamic approach and state-of-the-art catalysts. *J. Energy Chem.* **2020**, *48*, 54–91.
20. Olah, G.A.; Goeppert, A.; Czaun, M.; Mathew, T.; May, R.B.; Prakash, G.K.S. Single step bi-reforming and oxidative bi-reforming of methane (natural gas) with steam and carbon dioxide to metgas ($CO\text{-}2H_2$) for methanol synthesis: Self-sufficient effective and exclusive oxygenation of methane to methanol with oxygen. *J. Am. Chem. Soc.* **2015**, *137*, 8720–8729.
21. Olah, G.A.; Goeppert, A.; Czaun, M.; Prakash, G.K.S. Bi-reforming of methane from any source with steam and carbon dioxide exclusively to metgas ($CO\text{-}2H_2$) for methanol and hydrocarbon synthesis. *J. Am. Chem. Soc.* **2013**, *135*, 648–650.
22. Ganesh, I. Conversion of carbon dioxide into methanol-a potential liquid fuel: Fundamental challenges and opportunities (a review). *Renew. Sust. Energ. Rev.* **2014**, *31*, 221–257.
23. Bradford, M.C.J.; Vannice, M.A. CO_2 reforming of CH_4. *Catal. Rev.Sci. Eng.* **1999**, *41*, 1–42.
24. Scarlat, N.; Dallemand, J.F.; Fahl, F. Biogas: Developments and perspectives in Europe, Renew. Energy **2018**, *129*, 457–472.
25. Jabbour, K.; Saad, A.; Inaty, L.; Davidson, A.; Massiani, P.; El Hassan, N. Ordered mesoporous $Fe\text{-}Al_2O_3$ based-catalysts synthesized via a direct" one-pot" method for the dry reforming of a model biogas mixture. *Int. J. Hydrogen Energy* **2019**, *44*, 14889–14907.
26. Bezerra, D.M.; Lucrédio, A.F.; Valentini, A.; Assaf, E.M. Biogas reforming over Ni catalysts dispersed in different mixed oxides containing Zn^{2+}, Al^{3+} and Zr^{4+} cations. *Mater. Res. Bull.* **2018**, *102*, 186–195.
27. Habibi, N.; Wang, Y.; Arandiyan, H.; Rezaei, M. Effect of substitution by Ni in $MgAl_2O_4$ spinel for biogas dry reforming. *Int. J. Hydrogen Energy* **2017**, *42*, 24159–24168.
28. Rostrupnielsen, J.R.; Hansen, J.H.B. Hansen, CO_2-reforming of methane over transition metals. *J. Catal.* **1993**, *144*, 38–48.
29. Mesrar, F.; Kacimi, M.; Liotta, L.F.; Puleo, F.; Ziyad, M. Syngas production from dry reforming of methane over Ni/perlite catalysts: Effect of zirconia and ceria impregnation. *Int. J. Hydrogen Energy* **2018**, *42*, 17142–17155.
30. Moral, A.; Reyero, I.; Alfaro, C.; Bimbela, F.; Gandía, L.M. Syngas production by means of biogas catalytic partial oxidation and dry reforming using Rh-based catalysts. *Catal. Today* **2018**, *299*, 280–288.
31. Roy, P.S.; Park, C.S.; Raju, A.S.K.; Kim, K. Steam-biogas reforming over a metal-foam-coated $(Pd\text{-}Rh)/(CeZrO_2\text{-}Al_2O_3)$ catalyst compared with pellet type alumina-supported Ru and Ni catalysts. *J. CO_2 Util.* **2015**, *12*, 12–20.
32. Avraam, D.; Halkides, T.; Liguras, D.; Bereketidou, O.; Goula, M. An experimental and theoretical approach for the biogas steam reforming reaction. *Int. J. Hydrogen Energy* **2010**, *35*, 9818–9827.
33. Arbag, H.; Yasyerli, S.; Yasyerli, N.; Dogu, G.; Dogu, T. Enhancement of catalytic performance of Ni based mesoporous alumina by Co incorporation in conversion of biogas to synthesis gas. *Appl. Catal. Env.* **2016**, *198*, 254–265.
34. Goula, M.; Charisiou, N.; Siakavelas, G.; Tzounis, L.; Tsiaoussis, I.; Panagiotopoulou, P.; Goula, G.; Yentekakis, I. Syngas production via the biogas dry reforming reaction over Ni supported on zirconia modified with CeO_2 or La_2O_3 catalysts. *Int. J. Hydrogen Energy* **2017**, *42*, 13724–13740.
35. Charisiou, N.; Tzounis, L.; Sebastian, V.; Hinder, S.; Baker, M.; Polychronopoulou, K.; Goula, M. Investigating the correlation between deactivation and the carbon deposited on the surface of Ni/Al_2O_3 and $Ni/La_2O_3\text{-}Al_2O_3$ catalysts during the biogas reforming reaction. *Appl. Surf. Sci.* **2019**, *474*, 42–56.
36. de Llobet, S.; Pinilla, J.; Moliner, R.; Suelves, I. Relationship between carbon morphology and catalyst deactivation in the catalytic decomposition of biogas using Ni, Co and Fe based catalysts. *Fuel* **2015**, *139*, 71–78.
37. Appari, S.; Janardhanan, V.M.; Bauri, R.; Jayanti, S. Deactivation and regeneration of Ni catalyst during steam reforming of model biogas: An experimental investigation. *Int. J. Hydrogen Energy* **2014**, *39*, 297–304.
38. Jabbour, K.; El Hassan, N.; Davidson, A.; Massiani, P.; Casale, S. Characterizations and performances of Ni/diatomite catalysts for dry reforming of methane. *Chem. Eng. J.* **2015**, *264*, 351–358.
39. Koo, K.Y.; Roh, H.-S.; Seo, Y.T.; Seo, D.J.; Yoon, W.L.; Park, S.B. A highly effective and stable nano-sized $Ni/MgO\text{-}Al_2O_3$ catalyst for gas to liquids (GTL) process. *Int. J. Hydrogen Energy* **2008**, *33*, 2036–2043.
40. Koo, K.Y.; Roh, H.-S.; Seo, Y.T.; Seo, D.J.; Yoon, W.L.; Park, S.B. Combined H_2O and CO_2 reforming of CH_4 over nano-sized $Ni/MgO\text{-}Al_2O_3$ catalysts for synthesis gas production for gas to liquid (GTL): Effect of Mg/Al mixed ratio on coke formation. *Catal. Today* **2009**, *146*, 166–171.
41. Chen, C.; Wang, X.; Chen, X.; Liang, X.; Zou, X.; Lu, X. Combined steam and CO_2 reforming of methane over one-pot prepared Ni/La-Si catalysts. *Int. J. Hydrogen Energy* **2019**, *44*, 4780–4793.

42. Roh, H.-S.; Koo, K.Y.; Jeong, J.H.; Seo, Y.T.; Seo, D.J.; Seo, Y.-S.; Yoon, W.L.; Bin Park, S. Combined reforming of methane over supported Ni catalysts. *Catal. Lett.* **2007**, *117*, 85–90.
43. Roh, H.-S.; Koo, K.Y.; Yoon, W.L. Combined reforming of methane over co-precipitated Ni-CeO_2, Ni-ZrO_2 and Ni-$Ce_{0.8}Zr_{0.2}O_2$ catalysts to produce synthesis gas for gas to liquid (GTL) process. *Catal. Today* **2009**, *146*, 71–75.
44. Djaidja, A.; Libs, S.; Kiennemann, A.; Barama, A. Characterization and activity in dry reforming of methane on NiMg/Al and Ni/MgO catalysts. *Catal Today* **2006**, *113*, 194–200.
45. Jabbour, K.; Massiani, P.; Davidson, A.; Casale, S.; El Hassan, N. Ordered mesoporous "one-pot" synthesized Ni-Mg (Ca)-Al_2O_3 as effective and remarkably stable catalysts for combined steam and dry reforming of methane (CSDRM). *Appl. Catal. Env.* **2017**, *201*, 527–542.
46. Jabbour, K.; El Hassan, N.; Davidson, A.; Casale, S.; Massiani, P. Factors affecting the long-term stability of mesoporous nickel-based catalysts in combined steam and dry reforming of methane. *Catal. Sci. Technol.* **2016**, *6*, 4616–4631.
47. Singh, S.; Bahari, M.B.; Abdullah, B.; Phuong, P.T.; Truong, Q.D.; Vo, D.-V.N.; Adesina, A.A. Bi-reforming of methane on Ni/SBA-15 catalyst for syngas production: Influence of feed composition. *Int. J. Hydrogen Energy* **2018**, *43*, 17230–17243.
48. Singh, S.; Nguyen, T.D.; Siang, T.J.; Phuong, P.T.; Phuc, N.H.H.; Truong, Q.D.; Lam, S.S.; Vo, D.-V.N. Boron-doped Ni/SBA-15 catalysts with enhanced coke resistance and catalytic performance for dry reforming of methane. *Int. J. Hydrogen Energy* **2020**, *93*, 31–42.
49. Siang, T.J.; Pham, T.L.M.; Van Cuong, N.; Phuong, P.T.T.; Phuc, N.H.H.; Truong, Q.D.; Vo, D.-V.N. Combined steam and CO_2 reforming of methane for syngas production over carbon-resistant boron-promoted Ni/SBA-15 catalysts. *Microporous Mesoporous Mater.* **2018**, *262*, 122–132.
50. Siang, T.J.; Bach, L.G.; Singh, S.; Truong, Q.D.; Ho, V.; Phuc, N.H.H.; Alenazey, F.; Vo, D.-V.N. Methane bi-reforming over boron-doped Ni/SBA-15 catalyst: Longevity evaluation. *Int. J. Hydrogen Energy* **2019**, *44*, 20839–20850.
51. Atinafu, D.G.; Chang, S.J.; Kim, K.-H.; Dong, W.; Kim, S. A novel enhancement of shape/thermal stability and energy-storage capacity of phase change materials through the formation of composites with 3D porous (3, 6)-connected metal-organic framework. *Chem. Eng. J.* **2020**, *389*, 124430–124440.
52. Qiu, J.; Huo, D.; Xue, J.; Zhu, G.; Liu, H.; Xia, Y. Encapsulation of a phase-change material in nanocapsules with a well-defined hole in the wall for the controlled release of drugs. *Angew. Chem. Int. Ed.* **2019**, *58*, 10606–10611.
53. Akeiber, H.; Nejat, P.; Majid, M.Z.A.; Wahid, M.A.; Jomehzadeh, F.; Famileh, I.Z.; Calautit, J.K.; Hughes, B.R.; Zaki, S.A. A review on phase change material (PCM) for sustainable passive cooling in building envelopes. *Renew. Sust. Energ. Rev.* **2016**, *60*, 1470–1497.
54. Lei, C.; Wu, K.; Wu, L.; Liu, W.; Du, R.; Chen, F.; Fu, Q. Phase change material with anisotropically high thermal conductivity and excellent shape stability due to its robust cellulose/BNNSs skeleton. *J. Mater. Chem. A* **2019**, *7*, 19364–19373.
55. Imperor-Clerc, M.; Appay, M.-D.; Beaunier, P.; Davidson, A. Crystallization of β-MnO_2 nanowires in the pores of SBA-15 silicas: In situ investigation using synchrotron radiation. *Chem. Mater.* **2004**, *16*, 1813–1821.
56. Lopes, I.; El Hassan, N.; Guerba, H.; Wallez, G.; Davidson, A. Size-induced structural modifications affecting Co_3O_4 nanoparticles patterned in SBA-15 silicas. *Chem. Mater.* **2006**, *18*, 5826–5828.
57. Jabbour, K.; Kaydouh, M.; El Hassan, N.; El Zakhem, H.; Casale, S.; Massiani, P.; Davidson, A. Compared activity and stability of three Ni-silica catalysts for methane bi-and dry reforming, International Mediterranean Gas and Oil Conference. In Proceedings of the 2015 International Mediterranean Gas and Oil Conference (MedGO), Mechref, Lebanon, 16–18 April 2015; pp. 1–4.
58. Liu, Q.; Gao, J.; Zhang, M.; Li, H.; Gu, F.; Xu, G.; Zhong, Z.; Su, F. Highly active and stable Ni/γ-Al_2O_3 catalysts selectively deposited with CeO_2 for CO methanation. *RSC Adv.* **2014**, *4*, 16094–16103.
59. Liu, Q.; Gao, J.; Gu, F.; Lu, X.; Liu, Y.; Li, H.; Zhong, Z.; Liu, B.; Xu, G.; Su, F. One-pot synthesis of ordered mesoporous Ni-V-Al catalysts for CO methanation. *J. Catal.* **2015**, *326*, 127–138.
60. Xie, T.; Shi, L.; Zhang, J.; Zhang, D. Immobilizing Ni nanoparticles to mesoporous silica with size and location control via a polyol-assisted route for coking-and sintering-resistant dry reforming of methane. *Chem. Comm.* **2014**, *50*, 7250–7253.
61. Boudjahem, A.; Monteverdi, S.; Mercy, M.; Bettahar, M. Study of nickel catalysts supported on silica of low surface area and prepared by reduction of nickel acetate in aqueous hydrazine. *J. Catal.* **2004**, *221*, 325–334.
62. Ewald, S.; Standl, S.; Hinrichsen, O. Hinrichsen, Characterization of nickel catalysts with transient methods. *Appl. Catal. Gen.* **2018**, *549*, 93–101.
63. Trimm, D. The steam reforming of natural gas: Problems and some solutions. *Stud. Surf. Sci. Catal.* **1987**, *36*, 39–50.
64. Qin, D.; Lapszewicz, J. Study of mixed steam and CO_2 reforming of CH_4 to syngas on MgO-supported metals. *Catal. Today* **1994**, *21*, 551–560.
65. Koo, K.Y.; Lee, S.-H.; Jung, U.H.; Roh, H.-S.; Yoon, W.L. Syngas production via combined steam and carbon dioxide reforming of methane over Ni-Ce/$MgAl_2O_4$ catalysts with enhanced coke resistance. *Fuel Process. Technol.* **2014**, *119*, 151–157.
66. Koo, K.Y.; Jung, U.H.; Yoon, W.L. Combined H_2O and CO_2 reforming of CH_4 over Ce-promoted Ni/Al_2O_3 catalyst for gas to liquid (GTL) process: Enhancement of Ni-CeO_2 interaction. *Catal. Today* **2012**, *185*, 126–130.
67. Nagaoka, K.; Aika, K.; Seshan, K.; Lercher, J. Mechanism of carbon deposit/removal in methane dry reforming on supported metal catalysts. *Stud. Surf. Sci. Catal.* **2001**, *136*, 129–136.
68. Charisiou, N.D.; Siakavelas, G.I.; Tzounis, L.; Sebastian, V.; Stolojan, V.; Hinder, S.J.; Baker, M.A.; Polychronopoulou, K.; Goula, M.A. The relationship between reaction temperature and carbon deposition on nickel catalysts based on Al_2O_3, ZrO_2 or SiO_2 supports during the biogas dry reforming reaction. *Catalysts* **2019**, *9*, 676–698.

69. Kang, K.-M.; Shim, I.-W.; Kwak, H.-Y. Mixed and autothermal reforming of methane with supported Ni catalysts with a core/shell structure. *Fuel Process. Technol.* **2012**, *93*, 105–114.
70. Shamsi, A. Carbon formation on Ni-MgO catalyst during reaction of methane in the presence of CO_2 and CO. *Appl. Catal. Gen.* **2004**, *227*, 22–30.
71. Luo, J.Z.; Yu, Z.L.; Ng, C.F.; Au, C.T. CO_2/CH_4 reforming over Ni-La_2O_3/5A: An investigation on carbon deposition and reaction steps. *J. Catal.* **2000**, *194*, 198–210.
72. Guo, J.; Lou, H.; Zheng, X. The deposition of coke from methane on a Ni/$MgAl_2O_4$ catalyst. *Carbon* **2007**, *45*, 1314–1321.
73. Liu, D.; Quek, X.Y.; Cheo, W.N.E.; Lau, R.; Borgna, A.; Yang, Y. MCM-41 supported nickel-based bimetallic catalysts with superior stability during carbon dioxide reforming of methane: Effect of strong metal-support interaction. *J. Catal.* **2009**, *266*, 380–390.
74. Heise, H.M.; Kuckuk, R.; Ojha, A.K.; Srivastava, A.; Srivastava, V.; Asthana, B.P. Characterization of carbonaceous materials using Raman spectroscopy: A comparison of carbon nanotube filters, single-and multi-walled nanotubes, graphitised porous carbon and graphite. *J. Raman Spectrosc.* **2009**, *40*, 344–353.
75. Peter, J.F.; ChiáTsang, S. High-resolution electron microscopy of tubule-containing graphitic carbon. *J. Chem. Soc. Faraday Trans.* **1993**, *89*, 1189–1192.
76. Gu, G.; Wang, K.; Xiong, N.; Li, Z.; Fan, Z.; Hu, S.; Zou, X. Template free synthesis of lithium doped three-dimensional macroporous graphitic carbon nitride for photocatalytic N_2 fixation: The effect of Li-N active sites. *Dalton Trans.* **2019**, *48*, 5083–5089.
77. Ma, Q.; Han, Y.; Wei, Q.; Makpal, S.; Gao, X.; Zhang, J.; Zhao, T.-S. Stabilizing Ni on bimodal mesoporous-macroporous alumina with enhanced coke tolerance in dry reforming of methane to syngas. *J. CO_2 Util.* **2020**, *35*, 288–297.
78. Tong, G.; Wu, W.; Guan, J.; Qian, H.; Yuan, J.; Li, W. Synthesis and characterization of nanosized urchin-like α-Fe_2O_3 and Fe_3O_4: Microwave electromagnetic and absorbing properties. *J. Alloys Comp.* **2011**, *509*, 4320–4326.
79. Sehested, J.; Gelten, J.A.P.; Remediakis, I.N.; Bengaard, H.; Nørskov, J.K. Sintering of nickel steam-reforming catalysts: Effects of temperature and steam and hydrogen pressures. *J. Catal.* **2004**, *223*, 432–443.